Supplementary Information Appendix

for the article

CO_2 reduction driven by a pH gradient

Reuben Hudson*, Ruvan de Graaf, Mari Strandoo Rodin,
Aya Ohno, Nick Lane, Shawn E. McGlynn, Yoichi M.A. Yamada,
Ryuhei Nakamura, Laura M. Barge, Dieter Braun, Víctor Sojo*

Proc. Natl. Acad. Sci. USA (2020)

***Correspondence to:**

rhudson@coa.edu

vsojo@amnh.org

Contents

Supplementary figures

www.pnas.org/cgi/doi/10.1073/pnas.2002659117

Supplementary tables

1. The Wood-Ljungdahl acetyl-CoA pathway

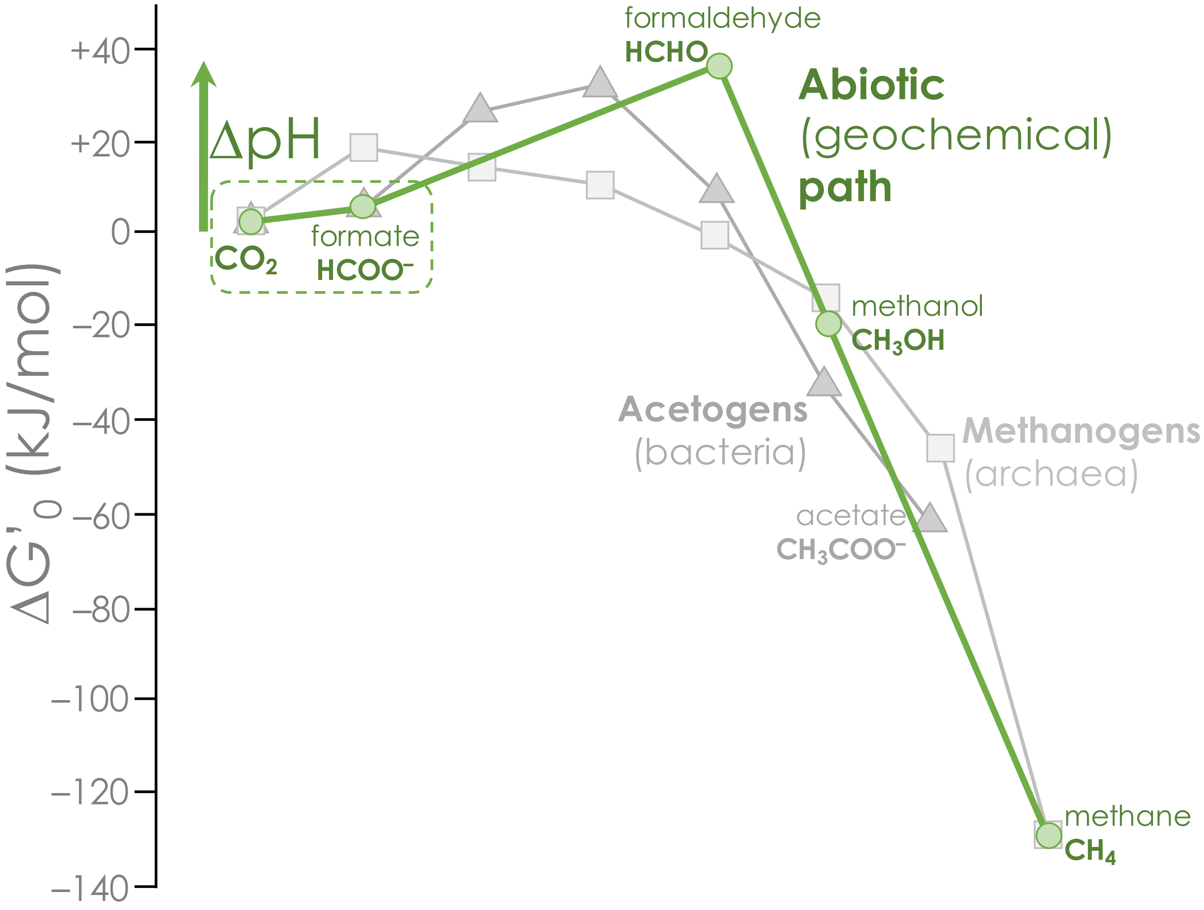

Figure S1. Energetic comparison between the full abiotic (and plausibly geochemical) reduction of CO_2 to methane (CH_4) and the Wood-Ljungdahl processes of acetogenesis (bacteria) and methanogenesis (archaea).

The reduction of CO_2 to formate (or the closely related carbon monoxide or formyl group) is common to a number of both abiotic and biotic carbon fixation processes. Once produced, formate can follow a rich variety of abiotic synthetic pathways. Here, one such geochemical fate of formate—the full reduction to methane, CH_4—is shown (green) in the context of the biotic Wood-Ljungdahl reductive acetyl Co-A pathways of methanogenesis (light gray) and acetogenesis (dark gray). The green arrow on the left shows the expected role of the pH gradient in overcoming the overpotentials for the syntheses of formate and formaldehyde. In the dashed box, the endergonic reaction demonstrated in this work. Adapted from Maden 2000 (1), Ragsdale & Pierce 2008 (2), and Yung et al. 2010 (3). Details of the acetogenic and methanogenic pathways in the cited literature.

2. Further Methods

2.1. Reactor parts and assembly

The reactor consisted of the following parts (see Figure S2):

- **Pressure-driven microfluidic pumps:** Dolomite Mitos P-pump (Dolomite part #:3200175)
- **Pump lids:** Mitos P-pump 3-way chamber lid (to enable seamless transition between different fluids on both the ocean and vent sides) (Dolomite part #: 3200044)
- **Valves:** 2-way in-line valves (Dolomite part #: 3200087)
- **Microfluidic chips:** Micronit H-Microreactor (borosilicate) (Micronit part #: 00755)
- **Microfluidic chip holder:** Micronit Fluidic Connect 4515 chipholder (part #: FC_FC4515)
- **T connectors:** Flow splitter 1/16” OD T-shape (3 connections) (Micronit part #: 01628)
- **In-line pH meters:** Sensorex pH electrode (Sensorex part #: 970277) with Modified Flow Cell FC49K, 50uL, PVDF (Sensorex part #: 970282).
- **Optical microscope:** Opti-Tekscope Digital USB Microscope Camera – Advanced CMOS Sensor, True High Definition Macro 200x Zoom Imaging

Figure S2. Reactor images

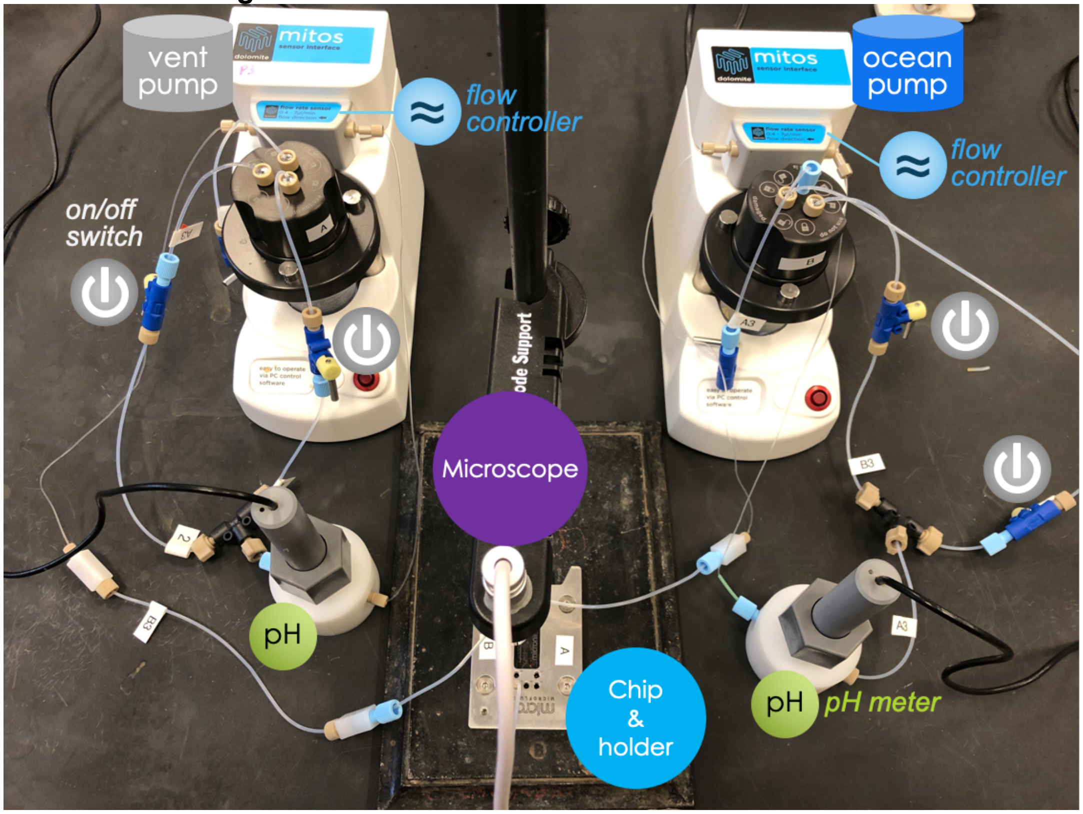

Note: For image clarity, the reactor has been assembled outside the glovebox. Please see safety notice in section 2.4 for further details.

The microfluidic reactor systems were assembled using borosilicate Y-junction chips (Micronit H-reactor). The channels in the system were half-pipes with a width of 300 ± 4.0 μm and a depth of 150 ± 5 μm. Simulants of ancient vent efflux and ocean fluids were entered at the two inputs of the Y-junction. A single, mixed output was collected. The fluid compositions, summarized in Table S1, were similar to those reported elsewhere (4–6). A general schematic of the reactor is provided in Figure 1B of the main text, and a photograph in Figure S2. A safety notice relating to work with pressurized H_2 is presented below in section 2.4.

In order to maximize the amount of dissolved gas (ocean side: CO_2; vent side H_2), we designed the microfluidic system to operate on gas pressure-driven pumps (Dolomite Mitos P-pump). Prior to driving the ocean and vent simulant fluids through the microfluidic device, we subjected the chambers to 10 pressurization-depressurization cycles (5 bar) in order to fully replace the headspace gas with the desired H_2 or CO_2. The final pressurization was held at the desired driving pressure (1.5 bar) for 10 min, prior to allowing the fluids to flow into the reactor.

To establish parallel flow prior to setting the Fe(Ni)S precipitate, we flowed the vent fluid (Na_2S, K_2HPO_4, $Na_2Si_3O_7$ in water; driven by H_2) alongside a metal-free ocean fluid (water; driven by CO_2), each at a flow rate of 5 μL/min. Control samples were taken at this point, resulting in no detectable product (presented as experiment #16 in Table 2 of the main text). Upon establishment of the parallel flow, we introduced the metal-containing ocean fluid ($FeCl_2$ and $NiCl_2$ in water; driven by CO_2). Invariably, within seconds of introducing the metal-containing ocean fluid, a black precipitate formed at the boundary of the laminar flow, which grew until the metal-containing ocean flow was replaced by the metal-free ocean flow (switched back to avoid the precipitate from growing to the point of occluding the channel). This switch from metal-containing to metal-free fluids typically occurred within 15-60 s of initial precipitate formation. Throughout the experiment, we maintained a flow rate of 5 μL/min for each the ocean- and vent-replicant fluids (10 μL/min overall combined flow).

Mimicking early-Earth anoxic conditions, both the vent efflux and ocean fluids were prepared in an N_2-purged glovebox with degassed, distilled water. To degas, water was sparged with N_2 for 30 min and subjected to three freeze-pump-thaw cycles. The gas-driven system we used is fully air-tight so, after preparation of the solutions in the anaerobic glovebox, the reaction was carried out outside. However, to provide an additional safety measure when working with pressurized H_2, the vent-side pump was housed within the N_2-purged glovebox throughout the experiment (see safety notice in section 2.4).

2.2. Maximum estimated dissolved H_2 and CO_2 concentrations

It was not possible in our system to determine the exact concentrations of dissolved H_2 and CO_2 in the vent and ocean fluids, respectively. However, using Henry's law, we estimate the maximum possible concentrations under our conditions to be 52 mM CO_2 and 1.2 mM H_2. Henry's law constants were obtained from the National Institute of Standards and Technology's WebBook at https://webbook.nist.gov, with ID=C124389 for CO_2 and ID=C1333740 for H_2.

2.3. Residence times and flow speeds

Given that the volume of the common channel of the chip is reported by the manufacturers as 0.55 μL, and that the fluids have a combined 10 μL/min flow rate (equivalent to 0.1667 μL/s), we calculate a total residence time of 3.3 s. The length of the common channel is reported as 14.8 mm, which gives a linear speed of 4.48 mm/s.

2.4. Safety notice

The Dolomite Mitos P-pumps are not designed for use with reactive gases (such as the highly combustible H_2). While the electronics are sealed away from the pressure chamber, a failed seal coupled with a spark from the electronics could result in H_2 combustion and rupture of the chamber. As a safety precaution, when using pressurized H_2 we operated the vent-side pump within a nitrogen-purged glovebox. This way, even if a pump seal failed and the electronics sparked, there would not be enough ambient O_2 to enable H_2 combustion.

2.5. Reagents and concentrations

- Iron (II) chloride tetrahydrate (99%) (Oakwood Chemicals).
- Nickel (II) chloride (98%) (Oakwood Chemicals).
- Sodium sulfide nonahydrate, ACS, (98.0% min) (Oakwood Chemicals).
- H_2 gas (UHP) (Maine Oxy).
- CO_2 gas (beverage grade: 99.95%) (Maine Oxy).
- N_2 gas (UHP) (Maine Oxy).
- Carbon-^{13}C Dioxide (99 Atom % ^{13}C) (Isotec/Sigma Aldrich).
- Deuterium (99.8 Atom %) (Isotec/Sigma Aldrich).
- K_2HPO_4 (ACS reagent > 98%) (Sigma Aldrich).
- K_3PO_4 (ACS reagent > 98%) (Sigma Aldrich).
- Na_2CO_3 (ACS reagent > 98%) (Sigma Aldrich).

Table S1. Ocean and vent analog default fluid compositions

Ocean-analog fluid		Vent-analog fluid	
$FeCl_2$	50 mM	Na_2S	100 mM
$NiCl_2$	5 mM	K_2HPO_4	10 mM
		$Na_2Si_3O_7$	10 mM
CO_2	1.5 bar	H_2	1.5 bar

Note: Once the precipitate was formed, the $FeCl_2$ and $NiCl_2$ were removed from the ocean-fluid input.

Reagents and concentrations were chosen to make our results directly comparable with previous work (4, 5, 7). As in those prior works, K_2HPO_4 was used as a buffer, and $Na_2Si_3O_7$ was added since it would have been present in relatively high concentrations in early-Earth waters (8), and because of its effect in stabilizing the precipitates demonstrated in previous work (9–11).

2.6. NMR analysis

Formate was identified using ^{1}H and ^{13}C NMR, and quantified using ^{1}H NMR. The post-chip effluent was centrifuged, of which 400 μL was added to an NMR tube with 100 μL of D_2O. For quantification, acetone was used as an internal standard (Figures Figure S3 and Figure S4), added immediately prior to analysis. Quantification was achieved by integration of the formyl peak in comparison against the known concentration for the six methyl protons of the acetone peak. The identity and concentration of formic acid were confirmed by spiking the outflow solution with additional formic acid, and noting the growth of the existing ^{1}H and ^{13}C peaks (Figure S3) rather than the introduction of new peaks (5). To confirm quantification results, re-integration of the formyl ^{1}H peak (8.42 ppm) in comparison with the acetone internal standard (2.22) followed after the known amount of additional formic acid was added. ^{1}H NMR spectra were conducted with water suppression for 256 scans. ^{13}C spectra were collected for 20,000-40,000 scans. Our limit of quantification for formate was 0.37 μM (see section 6). On a standard curve with acetone (0.6 μM) as an internal standard, concentrations of formate below this concentration deviated from linearity (0.037 μM & 0.0037 μM). NMR spectra were acquired on a Bruker 500 MHz NMR spectroscope.

3. ^{13}C NMR spectrum of Experiment 1

Figure S3. ^{13}C NMR spectrum of Experiment 1 efflux with and without formate spike
The tubes also contained acetone ($CH_3(CO)CH_3$).

Top: ^{13}C NMR spectrum of experiment 1 efflux.

Bottom: ^{13}C NMR spectrum of experiment 1 efflux after spiking with formate (increasing concentration by 2 μM). The growth of the formate peak (rather than introduction of a new peak) indicates that the original sample indeed contained formate.

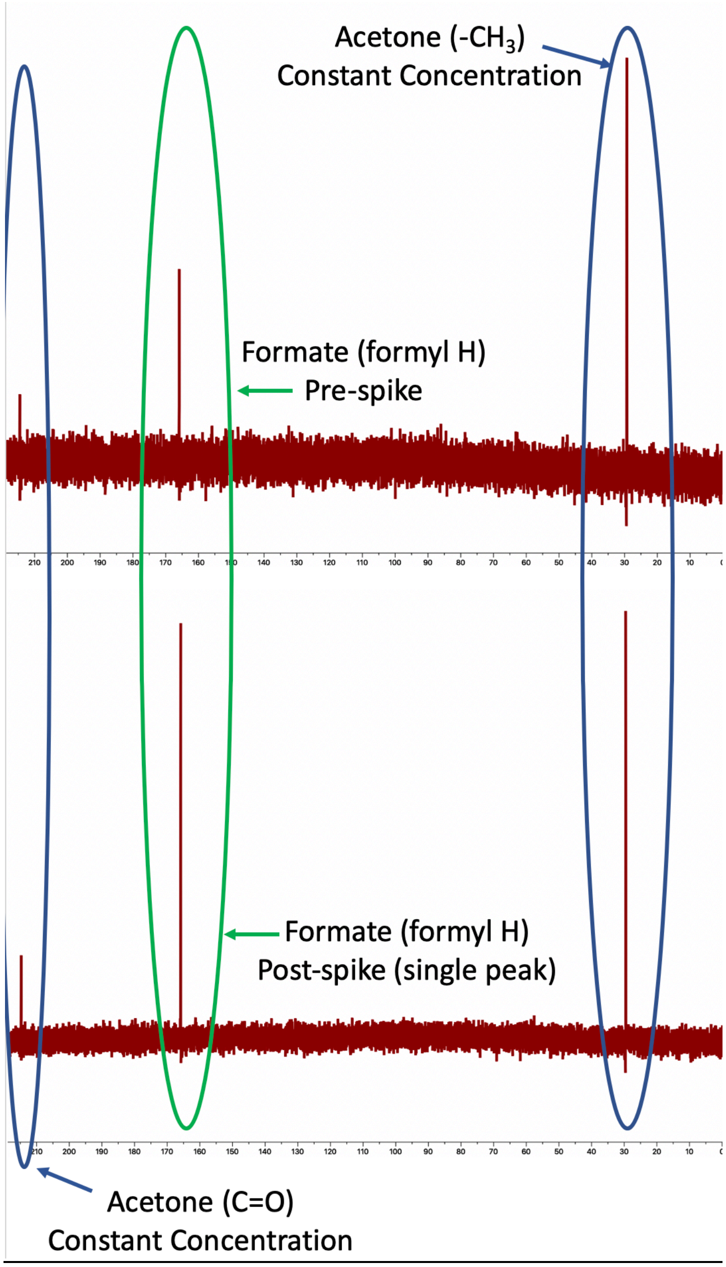

4. NMR reference spectra

Figure S4. Reference spectra of formic acid and acetone
NMR spectra of formic acid (98%) along with acetone internal standard.

(A) ^{1}H NMR spectrum.

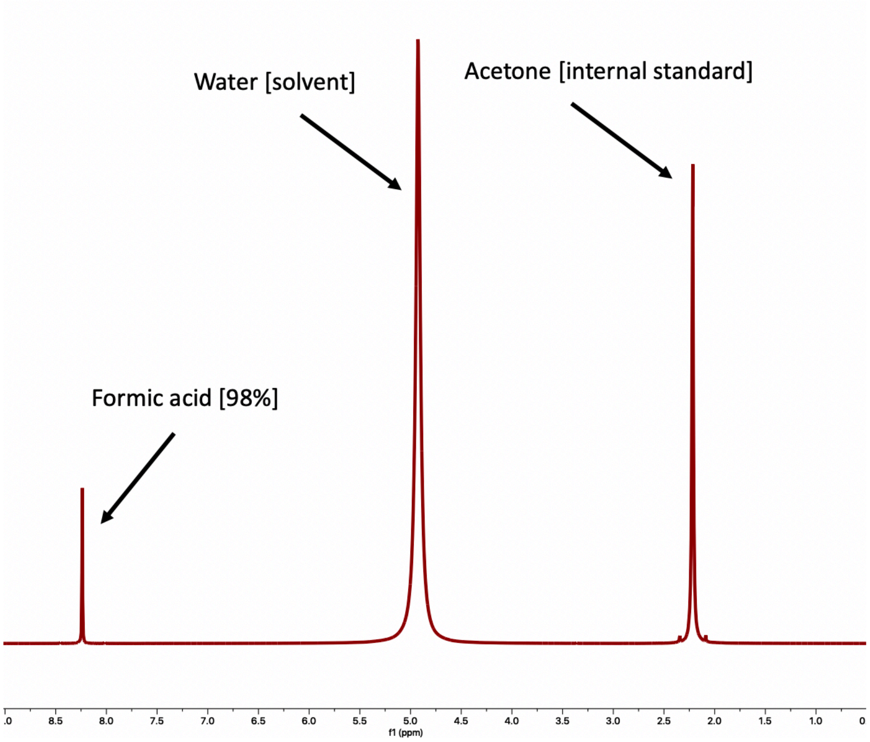

(B) ^{13}C NMR spectrum.

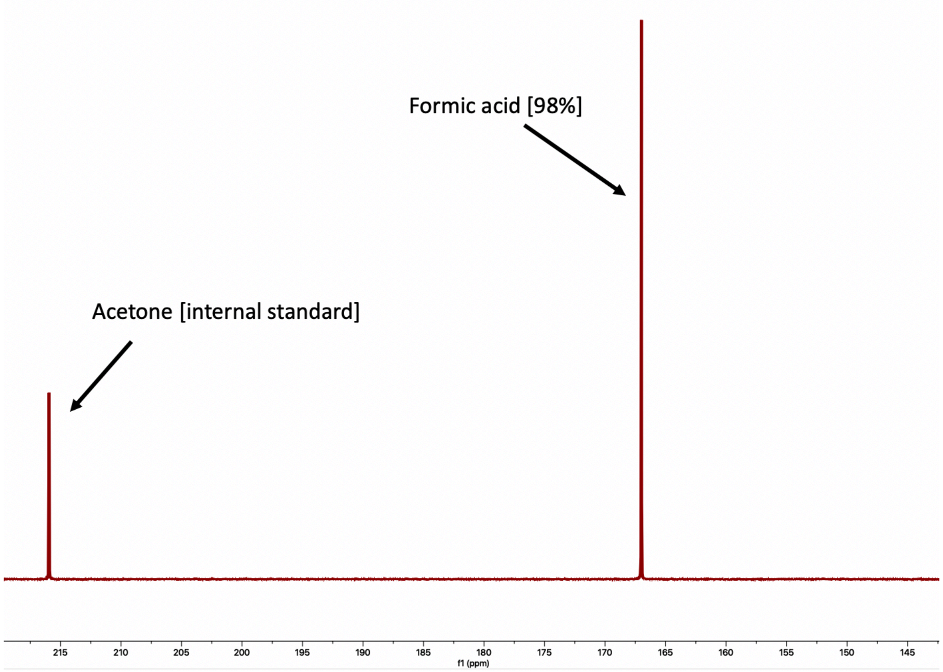

5. Further NMR details and quantification

Figure S5. ^{1}H NMR spectra of Experiment 1 with 0.6 μM acetone as an internal standard
(A) Integration of the acetone peak (1.00; 6 protons) relative to the formyl peak (0.46; 1 proton), indicates a 2 μM (1.656) concentration of formic acid.

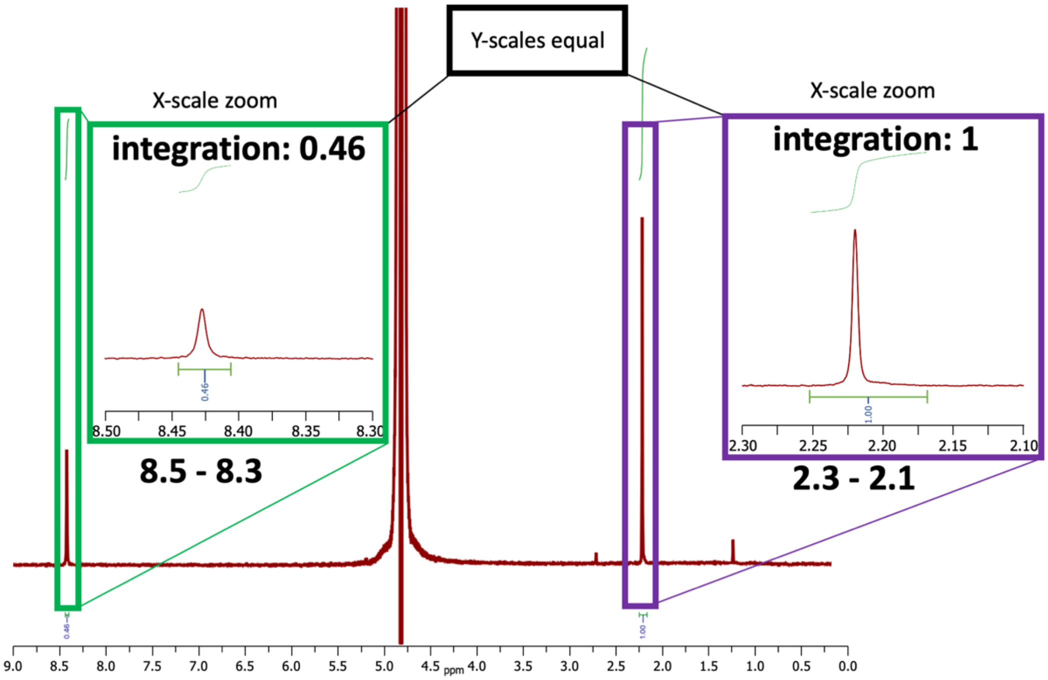

(B) Subsequent spiking of the previous sample (experiment 1) with a standard solution formic acid (raising concentration by an additional 2 μM), doubled the relative integration of the formyl peak (0.97) compared to the acetone peak (1.00). After spiking with a standard solution of formic acid, growth of a single peak, rather than introduction of a new peak, confirms the presence of formic acid in the original sample. Likewise, the magnitude of growth of the formate peak closely corresponds with the originally calculated concentration of formate. Pre-spike calculated formate concentration: 1.7 μM. Post-spike (2.0 μM) calculated formate concentration: 3.5 μM. Therefore, using the post/pre spike values to back-calculate the concentration of formate offers a value of 1.5 μM (3.5 – 2.0 = 1.5 μM).

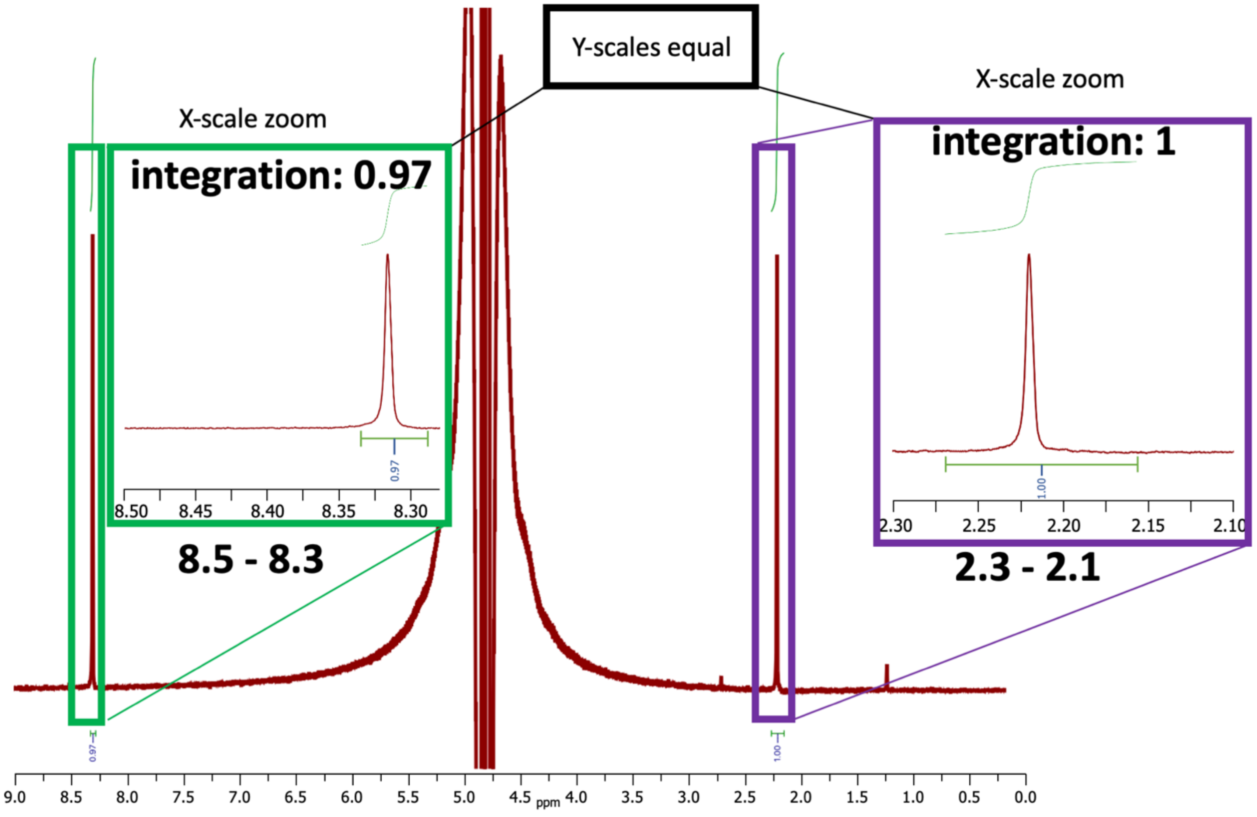

(C) Integration of the acetone peak (1.00; 6 protons) relative to the formyl peak (0.39; 1 proton), indicates a 1.404 μM concentration of formic acid.

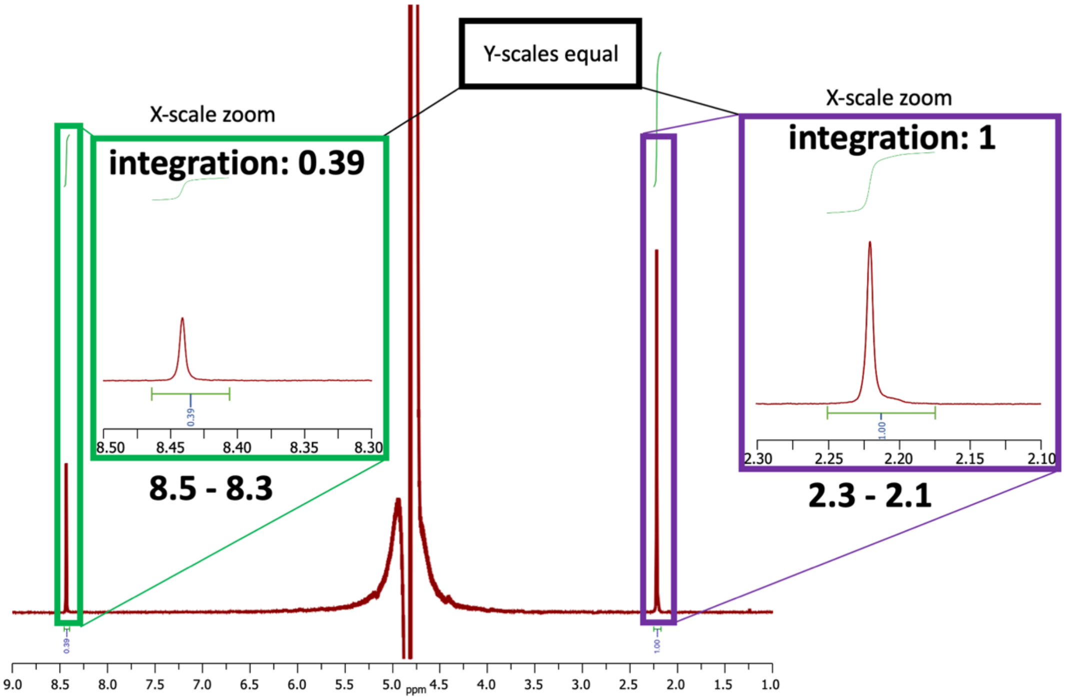

An average of the two experiment 1 samples indicates a 1.5 μM concentration of formic acid.

Figure S6. ^{1}H and ^{13}C NMR spectra of Experiment 2 ($^{13}CO_2$ as ocean-driving gas)

(A) ^{1}H NMR indicates splitting for formyl peak into a doublet. In the rest of our study, quantification of formate was conducted by comparing the integration of the formyl singlet against the integration of an acetone internal standard. Because the ^{13}C labeling splits the formyl singlet into a doublet, such a comparison would be unreliable in this case. This analysis therefore offers only identification of the $H^{13}COO^-$ product, but not quantification.

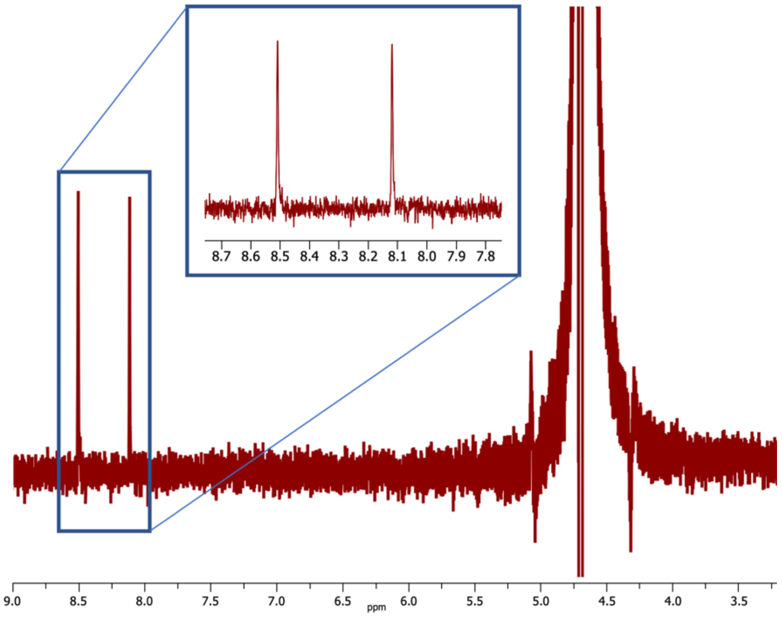

(B) ^{13}C NMR spectrum.

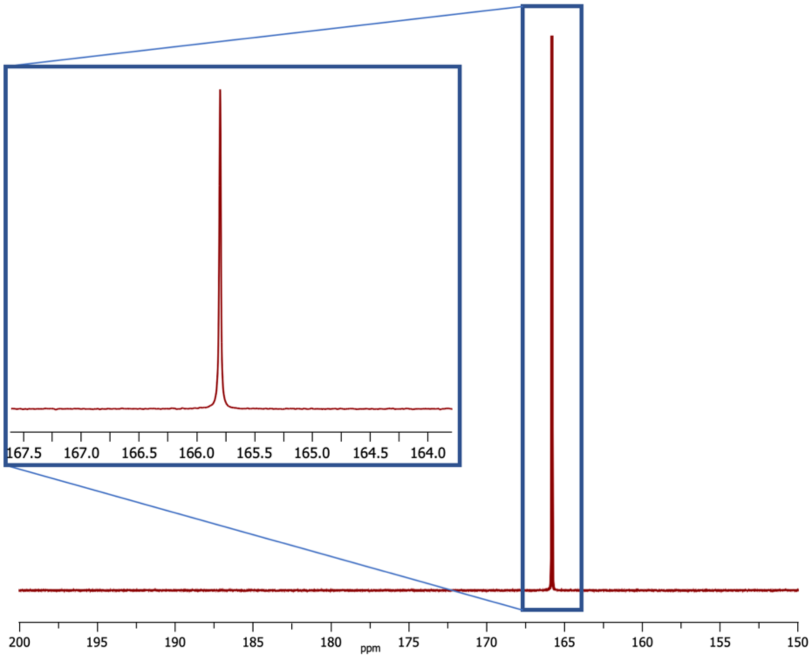

Figure S7. ^{1}H and ^{13}C NMR spectra of Experiment 3 (N_2 as vent-driving gas)

(A) The absence of any relevant peak (other than water) in the ^{1}H NMR spectrum indicates that no product was formed.

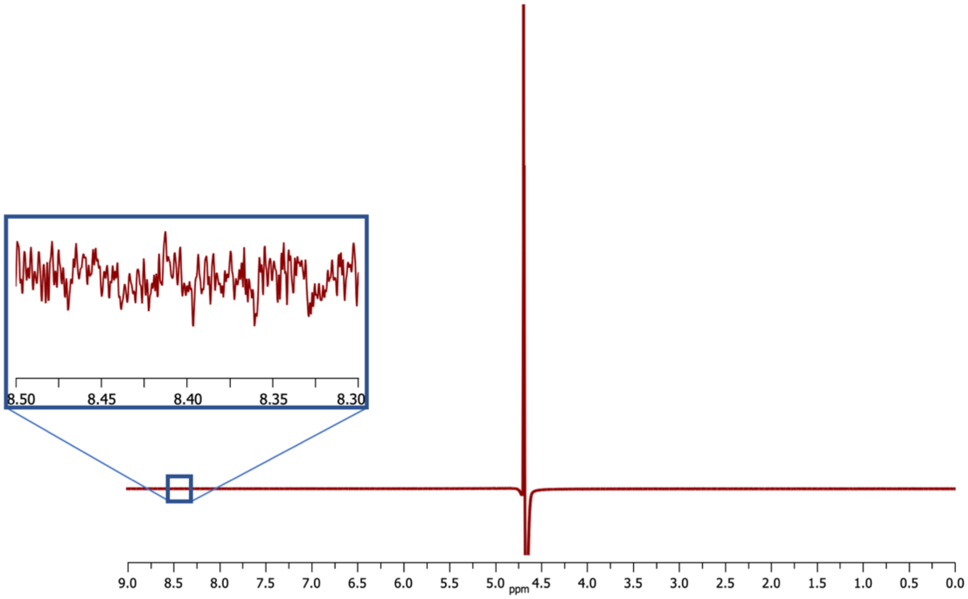

(B) No relevant peak in the ^{13}C NMR spectrum indicates that no product was formed appreciably.

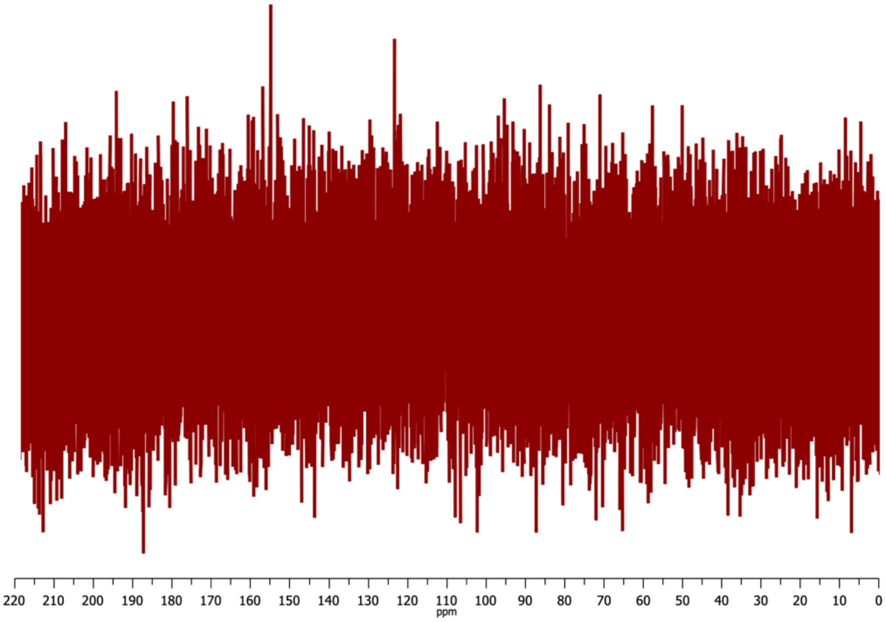

Figure S8. ^1H spectrum of Experiment 4 (D_2 as vent-driving gas)

(A) The formyl singlet indicates the presence of $HCOO^-$ rather than $DCOO^-$ (which would offer a doublet). Integration of the acetone peak (1.00; 6 protons) relative to the formyl peak (0.33; 1 proton), indicates a 1.2 μM concentration of formic acid.

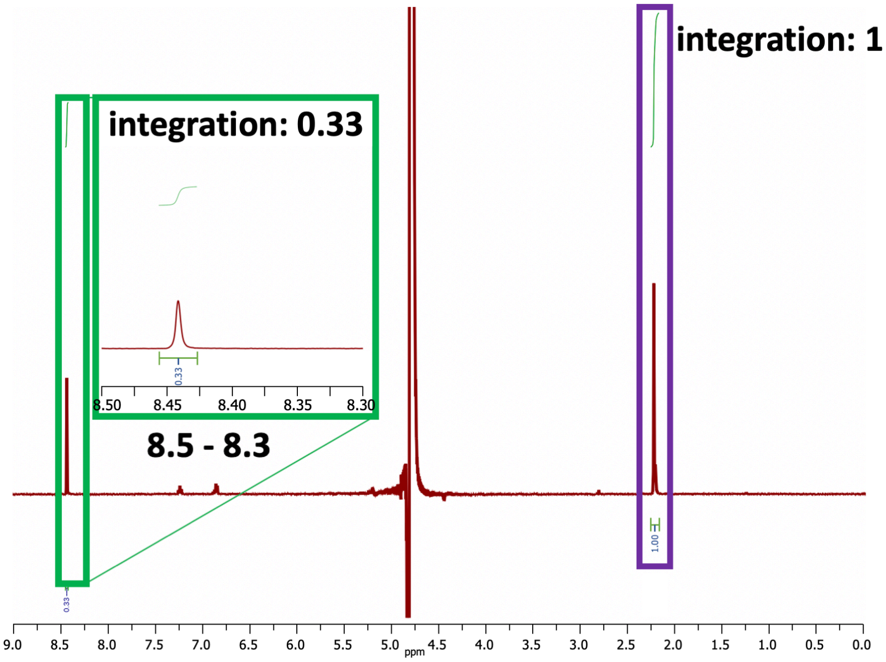

(B) In the above spectrum, the small peaks in 7.15–7.08 (t, 2H), and 6.76–6.71 (m, 3H) are consistent with trace contamination by an O- or N- monosubstituted benzene (where the *ortho*/*para* peaks would overlap to offer a multiplet with integration of 3H). The chemical shifts, splitting pattern and integration are consistent with either phenol or aniline. A magnification of these peaks appears below:

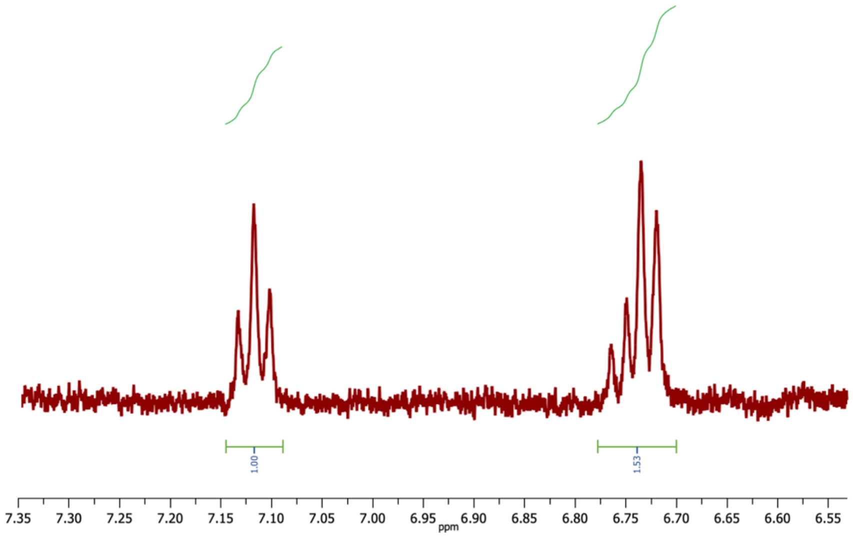

Figure S9. ^{1}H and ^{13}C NMR spectra of Experiment 5 (D_2O as ocean solvent)

(A) ^{1}H NMR indicates no formyl ^{1}H, which could mean either that no formate was produced at all, or instead, that the product is deuterium-labeled formate ($DCOO^-$)—as is indeed shown by the ^{13}C spectrum in panel B). In the rest of our study, quantification of formate was conducted by comparing the integration of the formyl singlet against the integration of an acetone internal standard. Because there is no formate peak, such quantification is not possible in this case. This analysis therefore offers only identification of the $DCOO^-$ product, but not quantification.

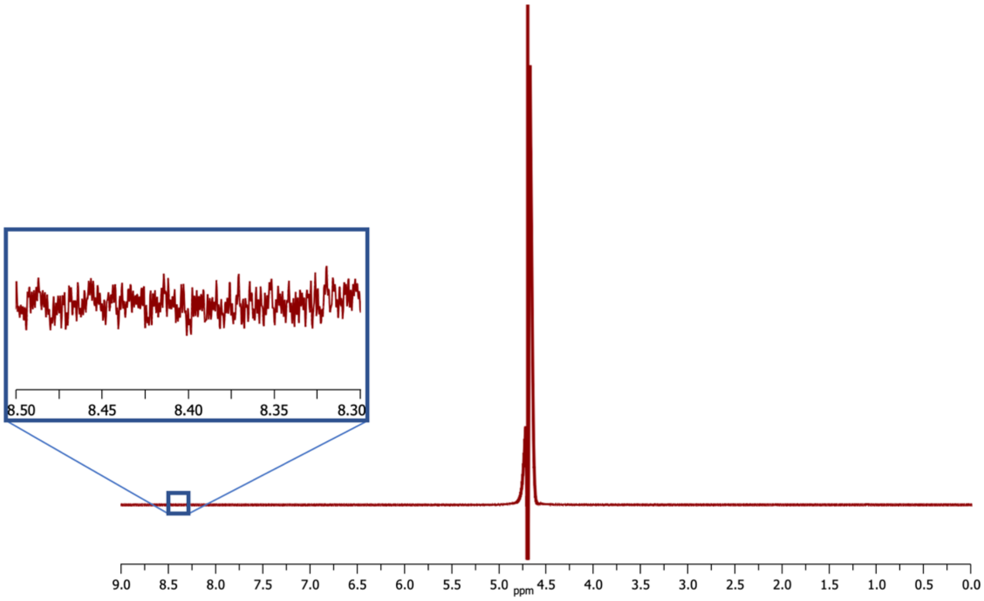

(B) ^{13}C NMR spectrum indicates splitting of the singlet into a triplet—consistent with D-C coupling.

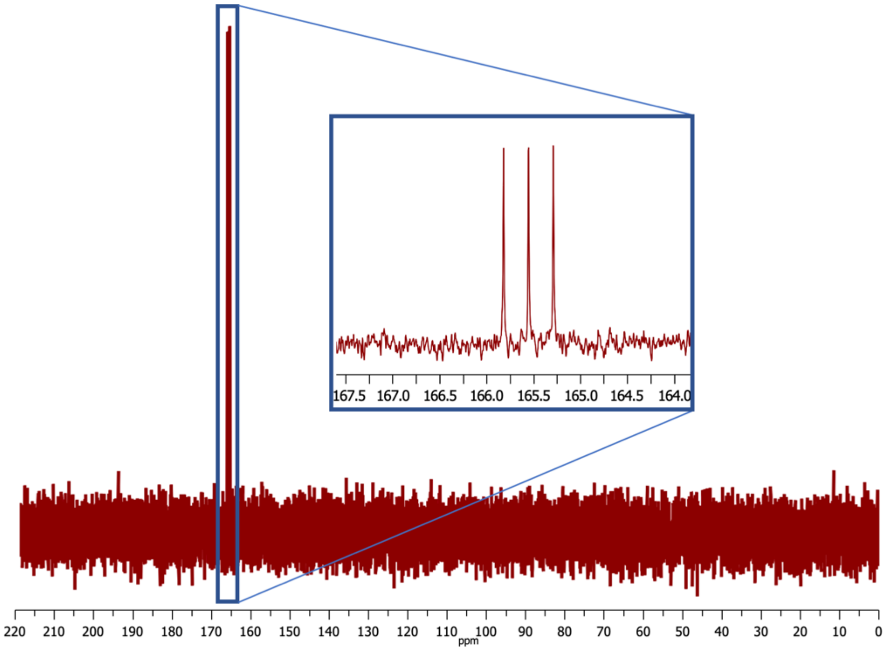

Figure S10. ^{1}H NMR spectra of Experiment 6 (no solutes on vent-side)
Acetone 0.6 µM was added as an internal standard.

(A) No formate peak was observed.

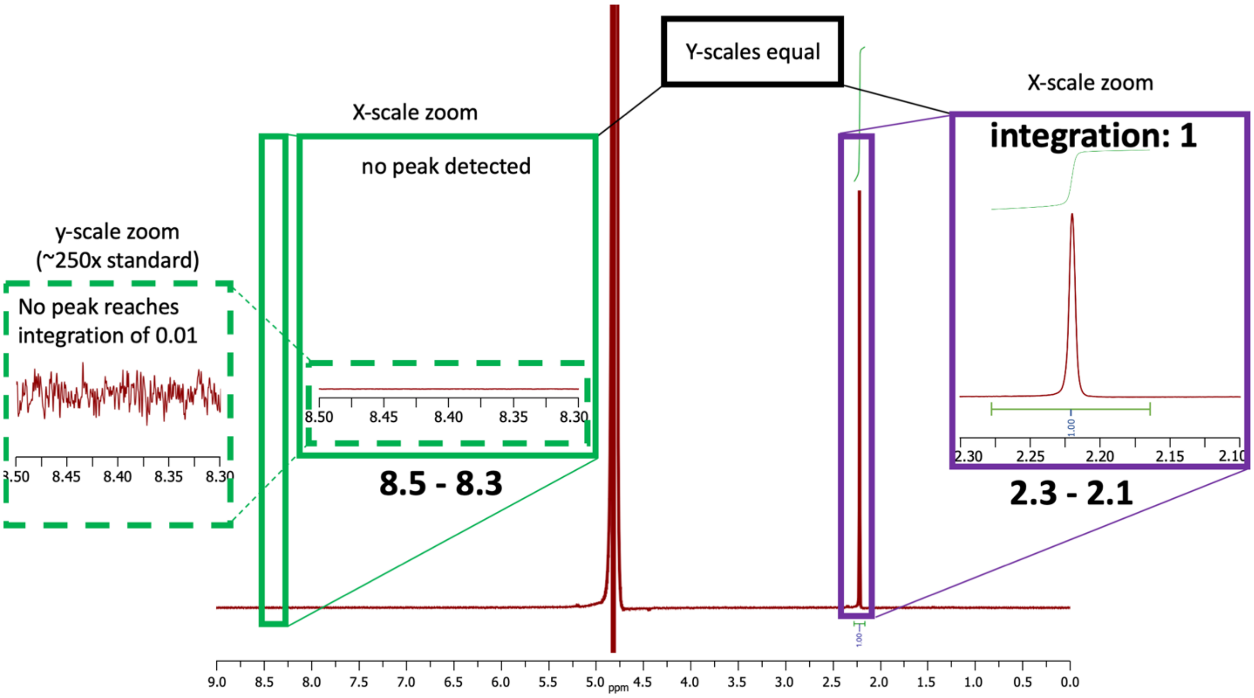

(B) Duplicate. No formate peak was observed.

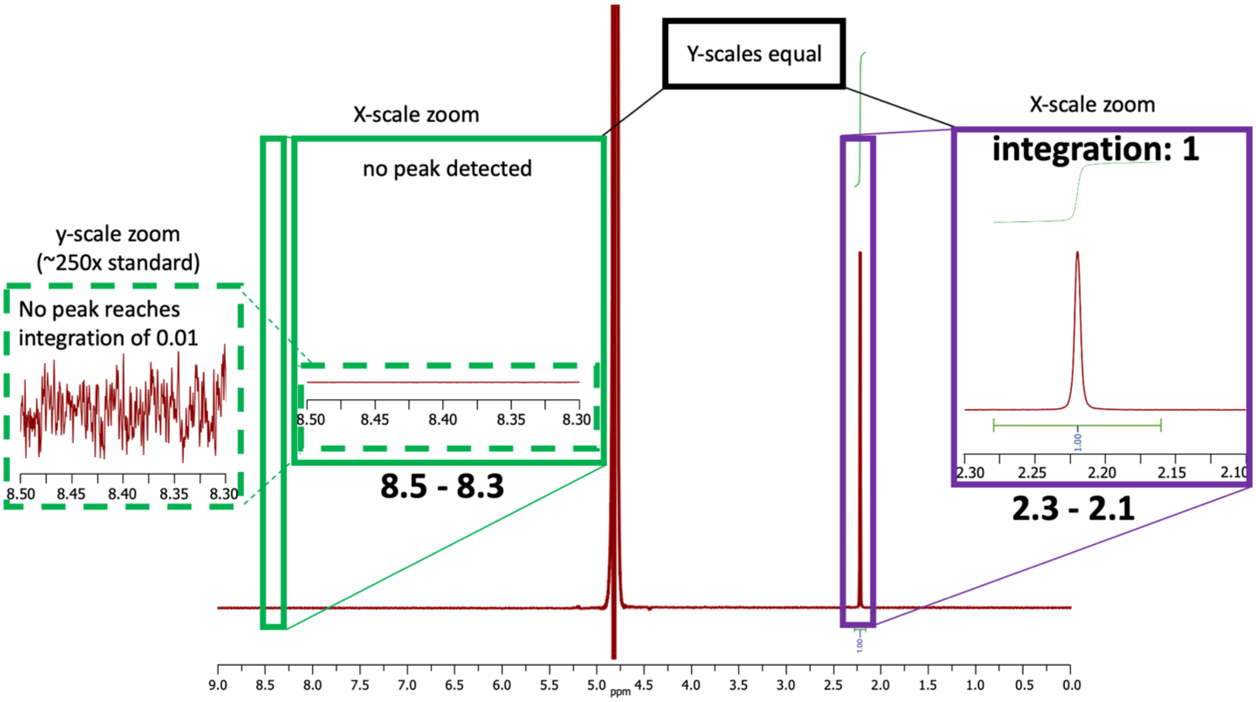

Figure S11. ^{1}H NMR spectra of Experiment 7 (vent-side titrated to pH 7.0)
Acetone 0.6 µM was added as an internal standard.

(A) No formate peak was observed.

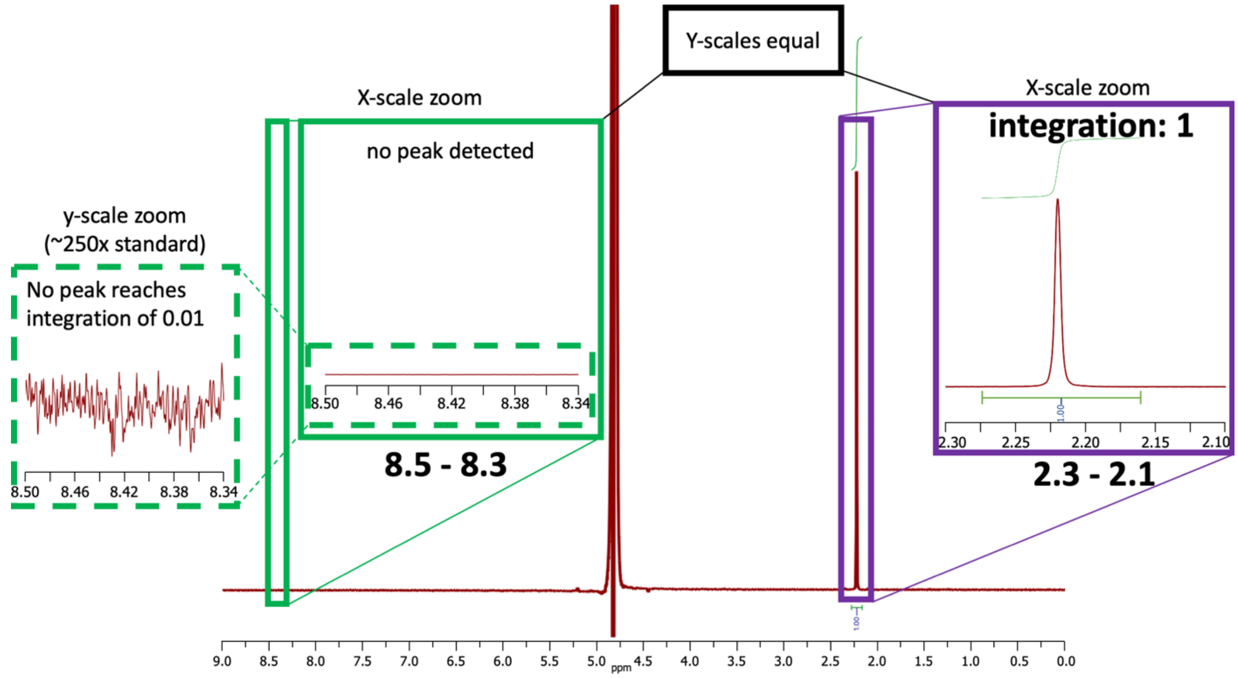

(B) Duplicate. No formate peak was observed.

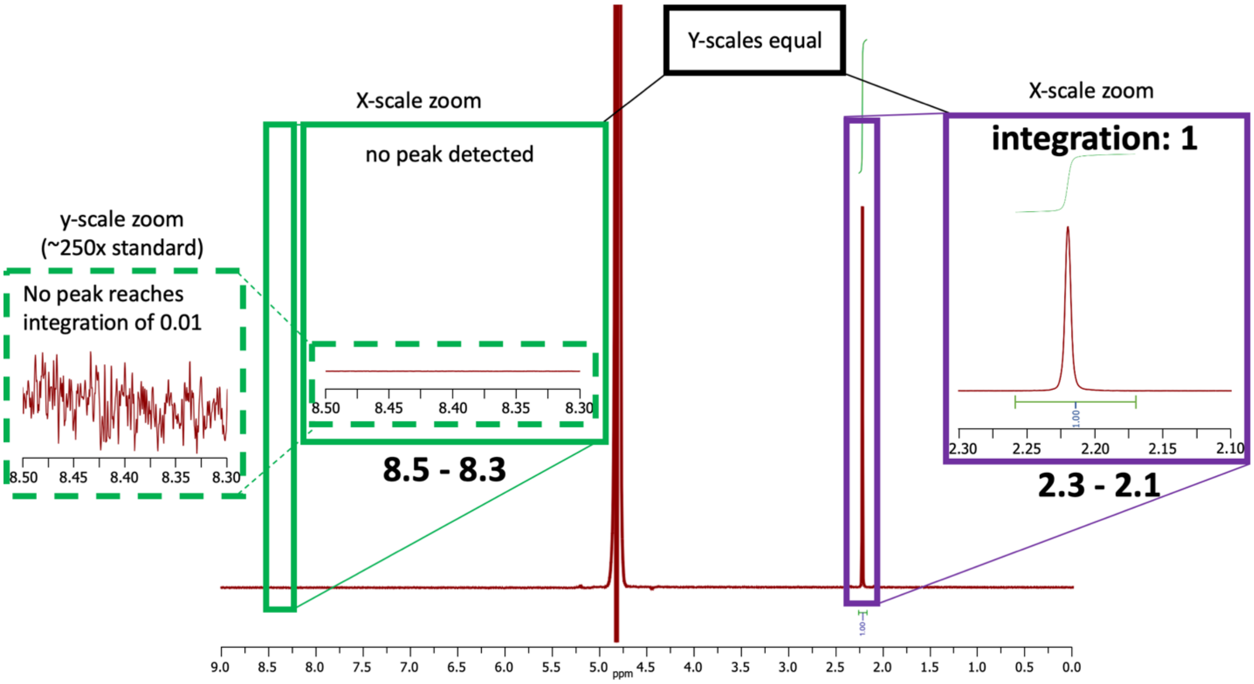

Figure S12. ^{1}H NMR spectra of Experiment 8 (vent-side titrated to pH 3.9)
Acetone 0.6 µM was added as an internal standard.

(A) No formate peak was observed.

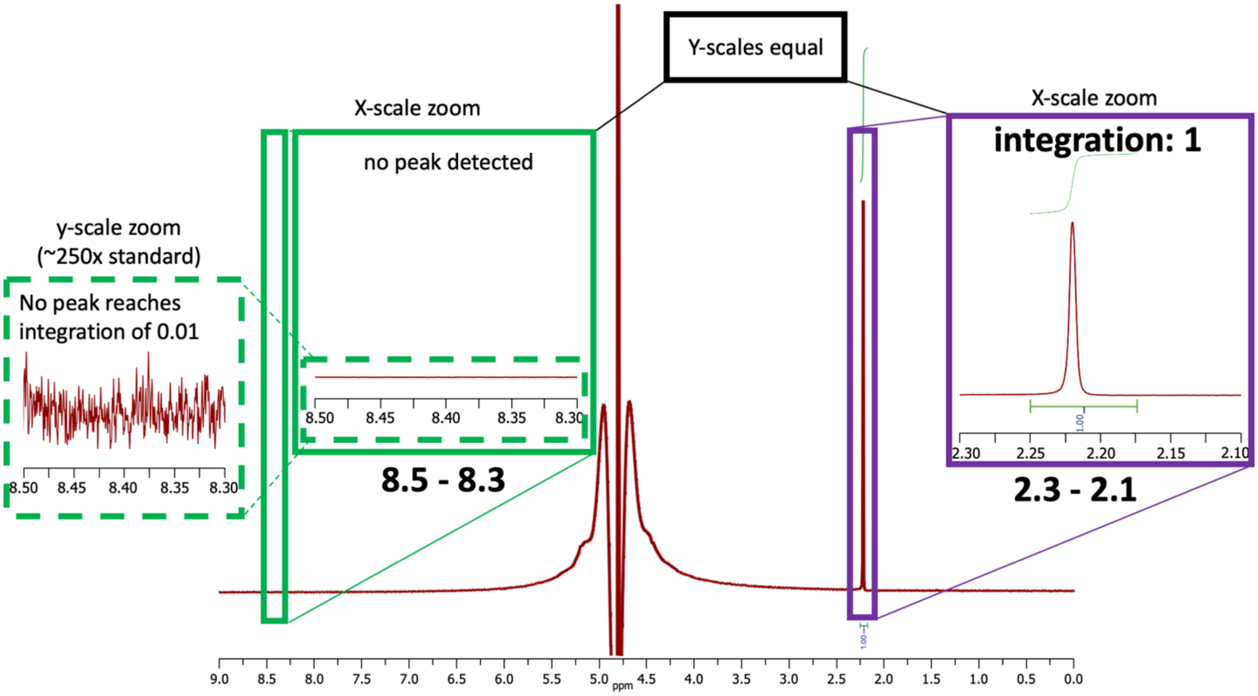

(B) Duplicate. No formate peak was observed.

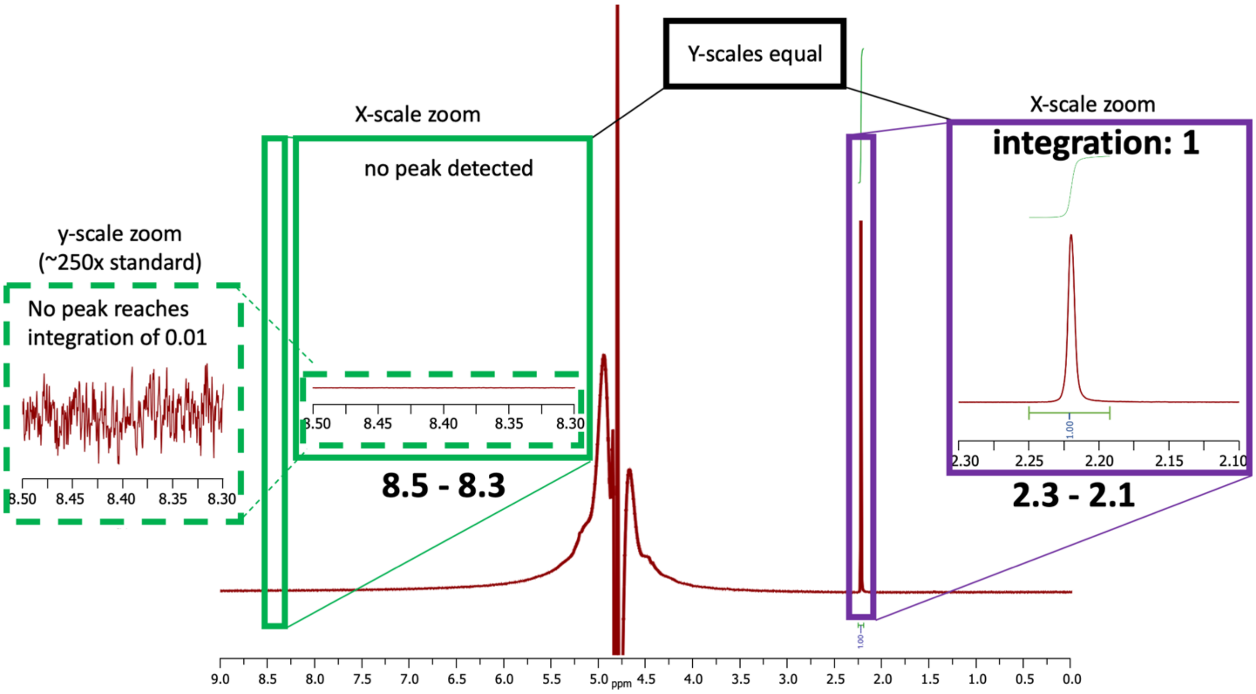

Figure S13. ^{1}H NMR spectra of Experiment 9 (Na_2CO_3 in ocean fluid)
Acetone 0.6 μM was added as an internal standard.

(A) No formate peak was observed.

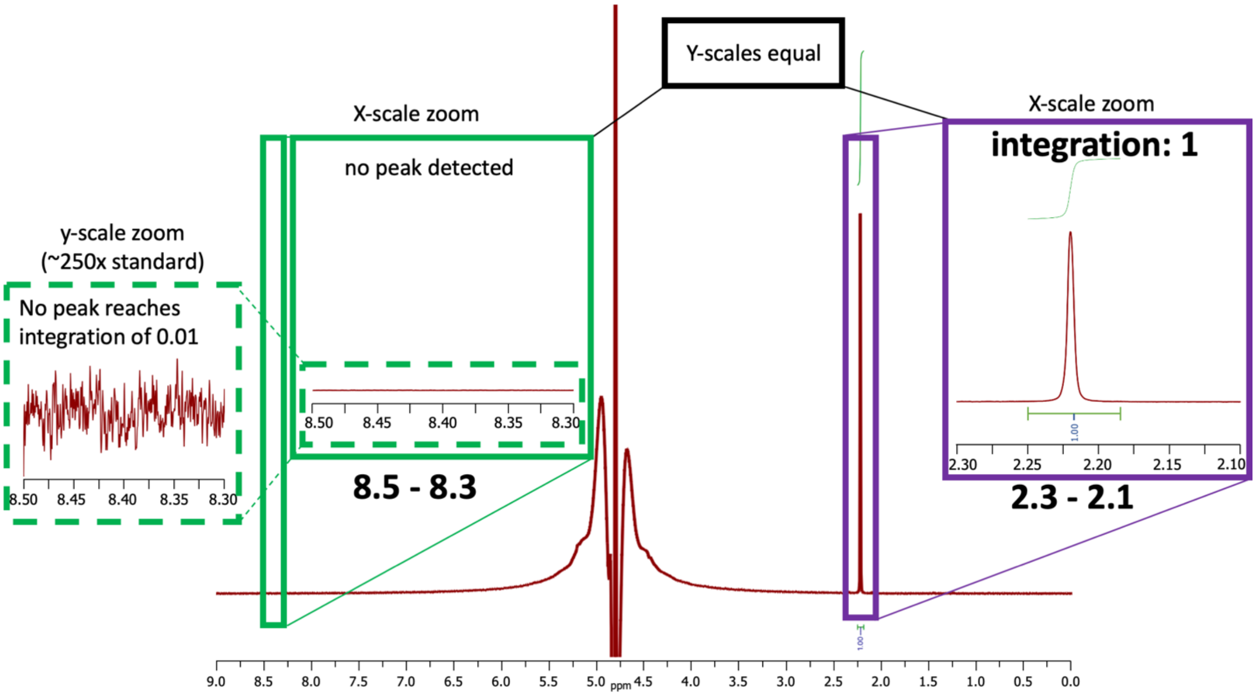

(B) Duplicate. No formate peak was observed.

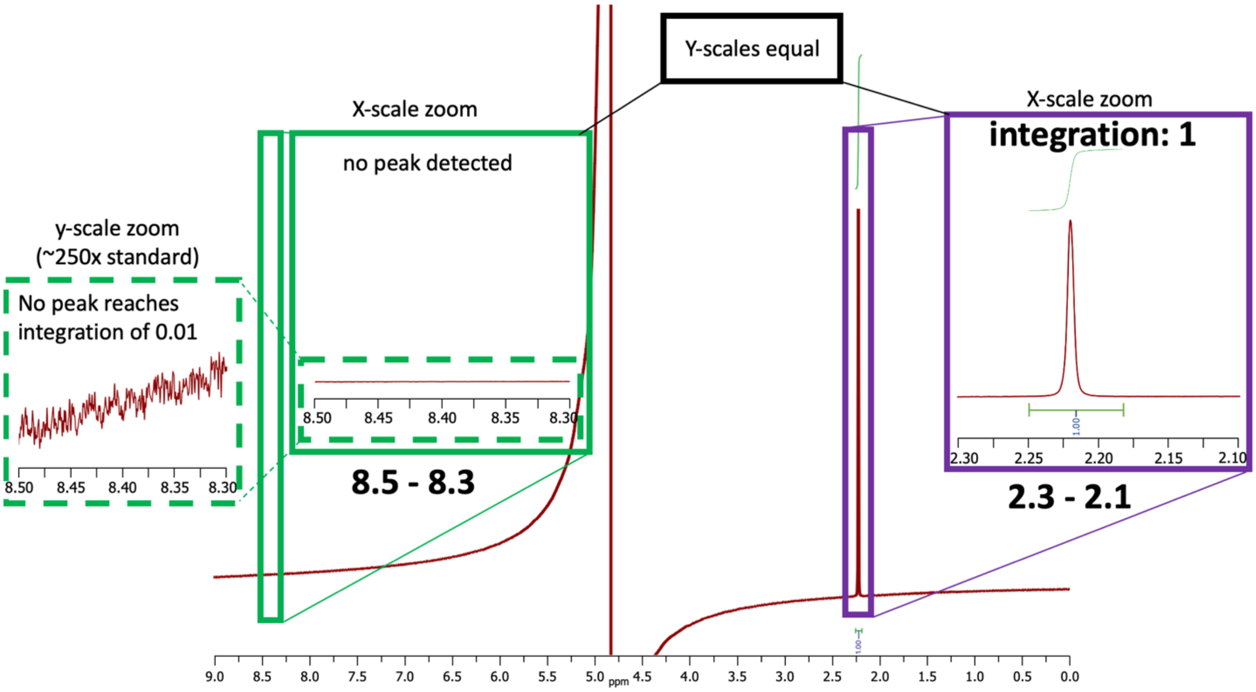

Figure S14. ^{1}H NMR spectra of Experiment 10 (no $Na_2Si_3O_7$ in vent post-precipitation fluid) Acetone 0.6 µM was added as an internal standard.

(A) Integration of the acetone peak (1.00; 6 protons) relative to the formyl peak (0.37; 1 proton), indicates a 1.332 µM concentration of formic acid.

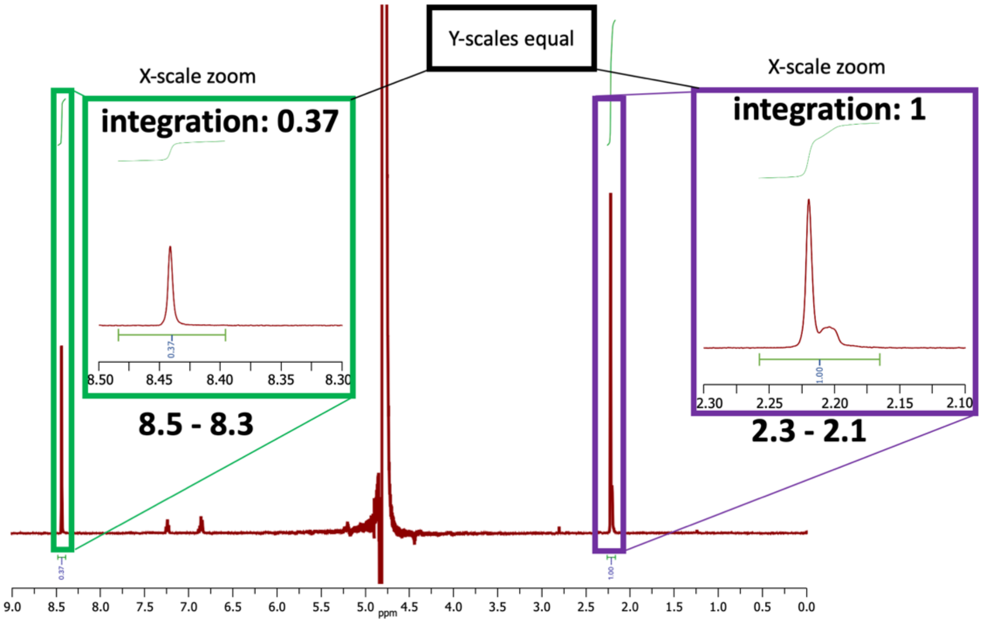

(B) Duplicate. Integration of the acetone peak (1.00; 6 protons) relative to the formyl peak (0.47; 1 proton), indicates a 1.692 µM concentration of formic acid.

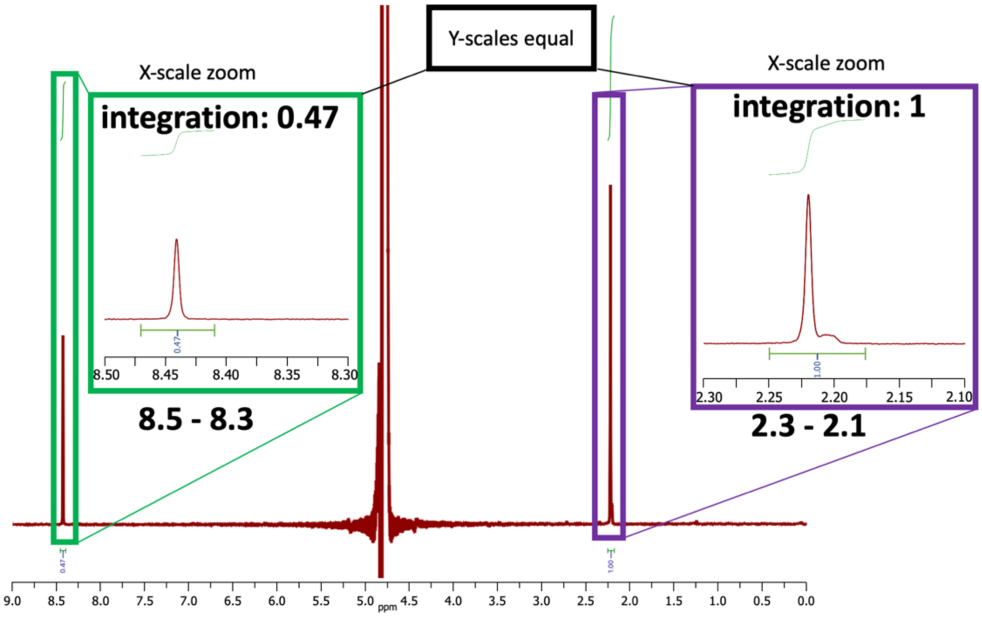

An average of the two samples indicates a 1.5 µM concentration of formic acid. A small broad peak in the alkyl region (2.19–2.21 ppm), observed also in Figure S15, Figure S18-Figure S19, will require further analysis.

Figure S15. ^{1}H NMR spectra of Experiment 11 (only Na_2S in vent post-precipitation fluid)
Acetone 0.6 µM was added as an internal standard.

(A) Integration of the acetone peak (1.00; 6 protons) relative to the formyl peak (0.59; 1 proton), indicates a 2.124 µM concentration of formic acid.

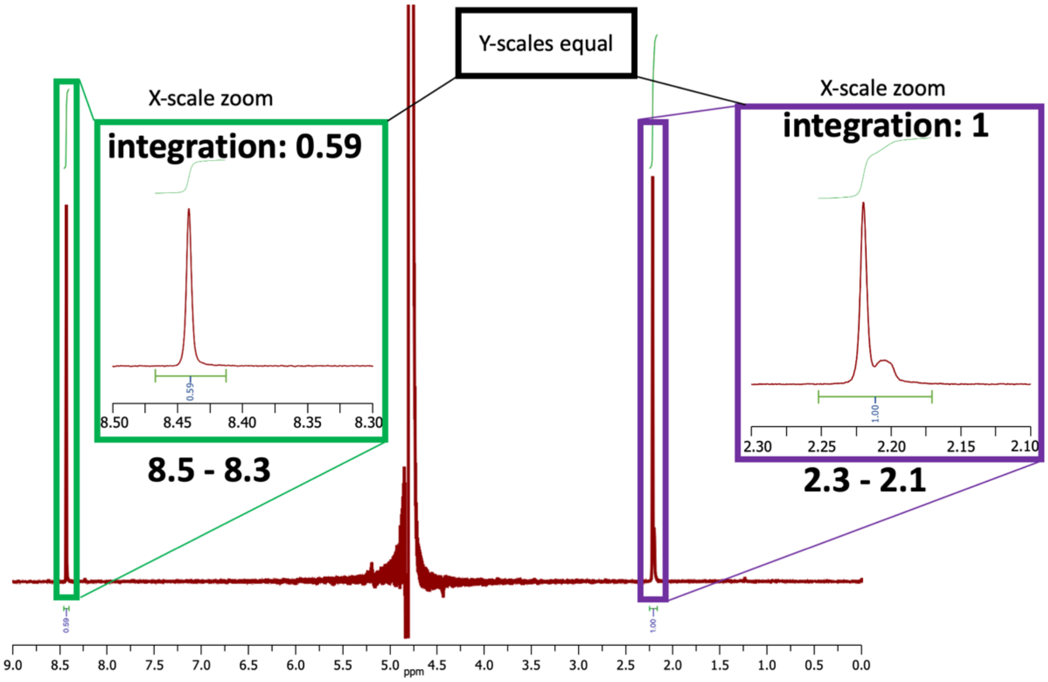

(B) Duplicate. Integration of the acetone peak (1.00; 6 protons) relative to the formyl peak (0.40; 1 proton), indicates a 1.440 µM concentration of formic acid.

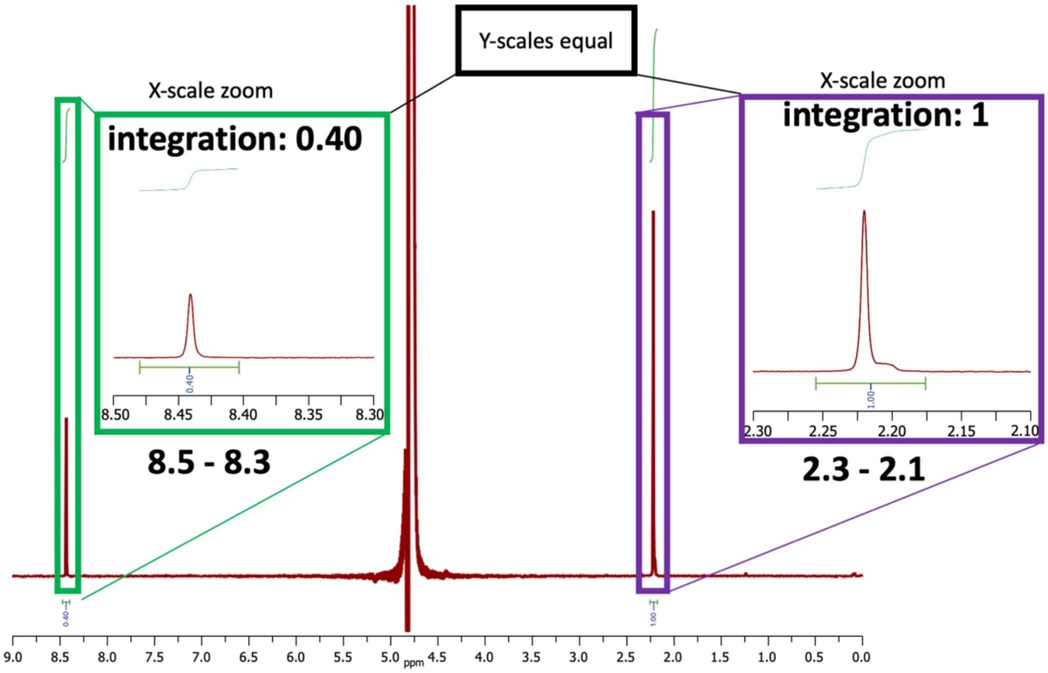

An average of the two samples indicates a 1.8 μM concentration of formic acid. A small broad peak in the alkyl region (2.19–2.21 ppm), observed also in Figure S14, Figure S18-Figure S19, will require further analysis.

Figure S16. ^{1}H NMR spectra of Experiment 12 (only K_2HPO_4 in vent post-precipitation fluid) Acetone 0.6 µM was added as an internal standard.

(A) Integration of the acetone peak (1.00; 6 protons) relative to the formyl peak (0.01; 1 proton), indicates that the formate peak is lower than the limit of quantification (see section 6)

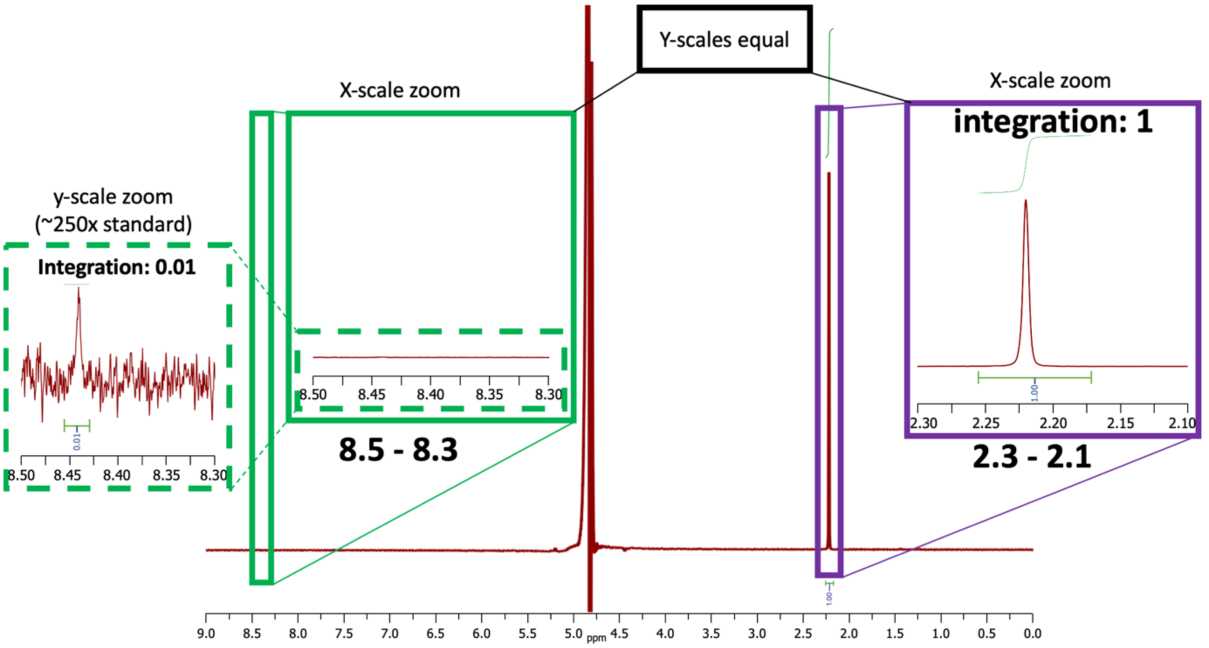

(B) Duplicate. Integration of the acetone peak (1.00; 6 protons) relative to the formyl peak (0.01; 1 proton), indicates that the formate peak is lower than the limit of quantification (see section 6).

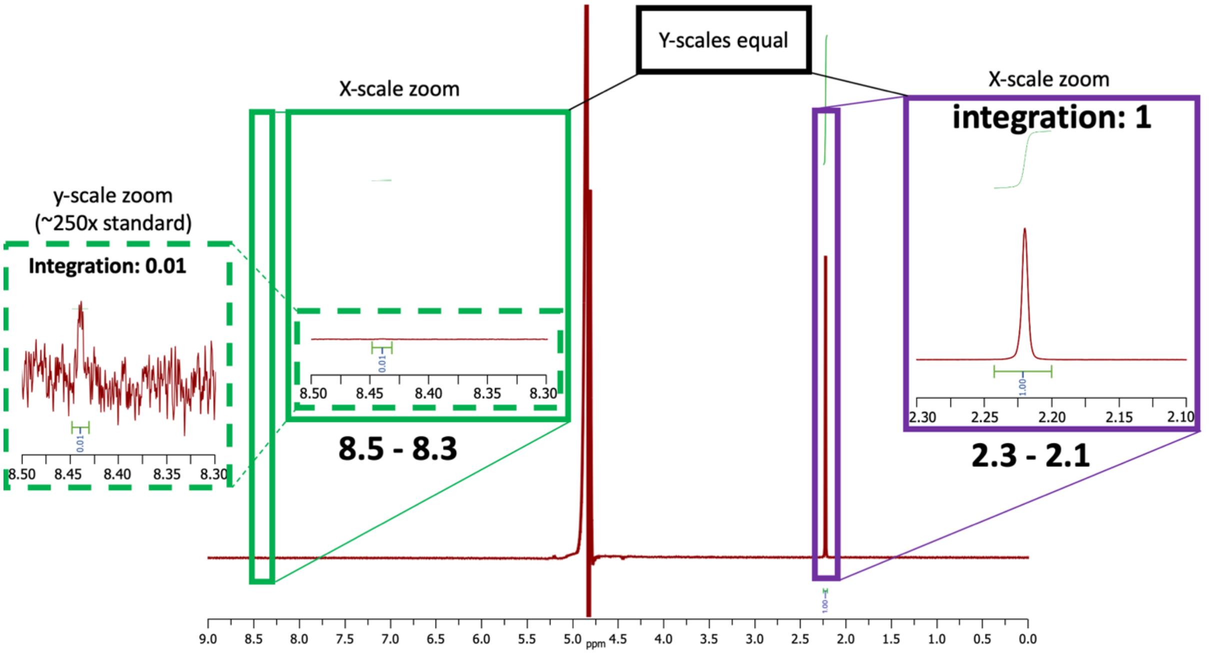

Both samples indicate formate above the detection limit, but below the limit of quantification (see section 6).

Figure S17. ^{1}H NMR spectra of Experiment 13 (only K_3PO_4 in vent post-precipitation fluid) Acetone 0.6 µM was added as an internal standard.

(A) Integration of the acetone peak (1.00; 6 protons) relative to the formyl peak (0.29; 1 proton), indicates a 1.044 µM concentration of formic acid.

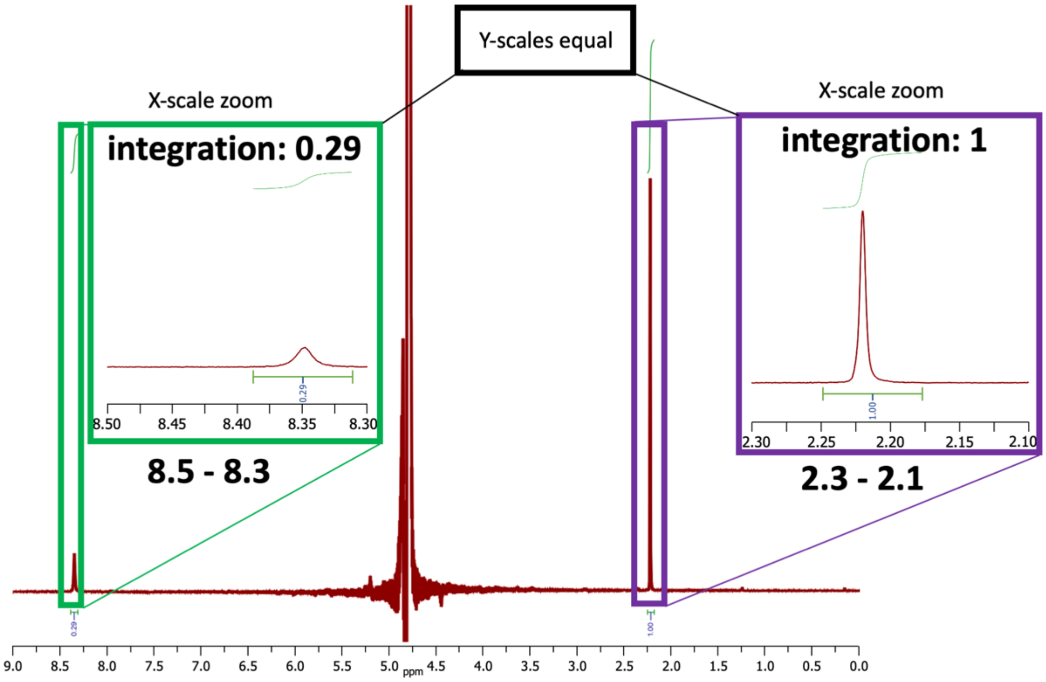

(B) Duplicate. Integration of the acetone peak (1.00; 6 protons) relative to the formyl peak (0.21; 1 proton), indicates a 0.756 µM concentration of formic acid.

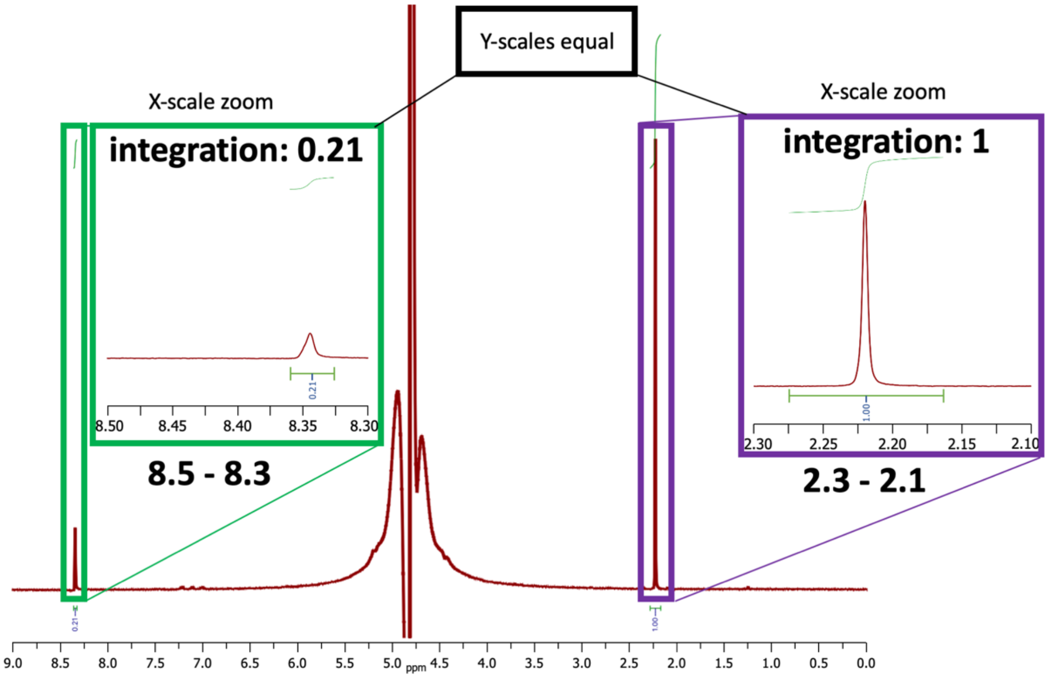

An average of the two samples indicates a 0.90 µM concentration of formic acid.

Figure S18. ^{1}H NMR spectra of Experiment 14 (only $FeCl_2$ in ocean precipitation fluid)
$NiCl_2$ was removed from the ocean precipitation fluid.

Acetone 0.6 μM was added as an internal standard.

(A) Integration of the acetone peak (1.00; 6 protons) relative to the formyl peak (0.03; 1 proton), indicates that the formate peak is lower than the limit of quantification (see section 6).

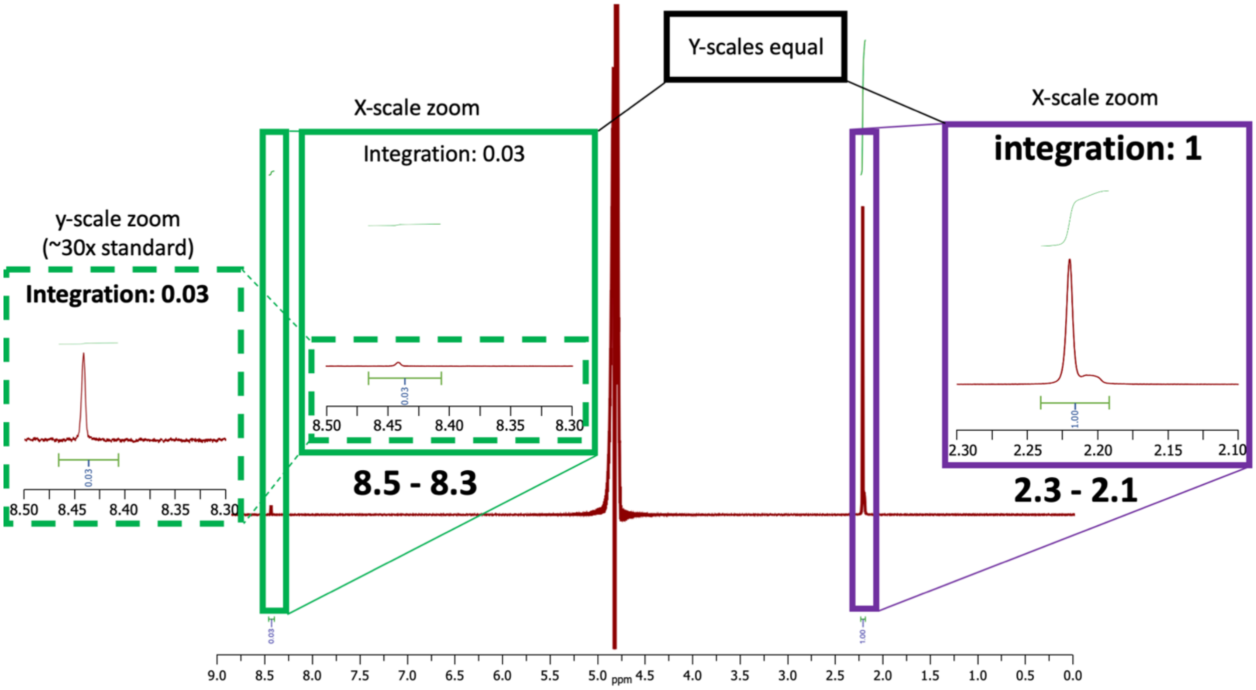

(B) Duplicate. Integration of the acetone peak (1.00; 6 protons) relative to the formyl peak (0.02; 1 proton), indicates that the formate peak is lower than the limit of quantification (see section 6).

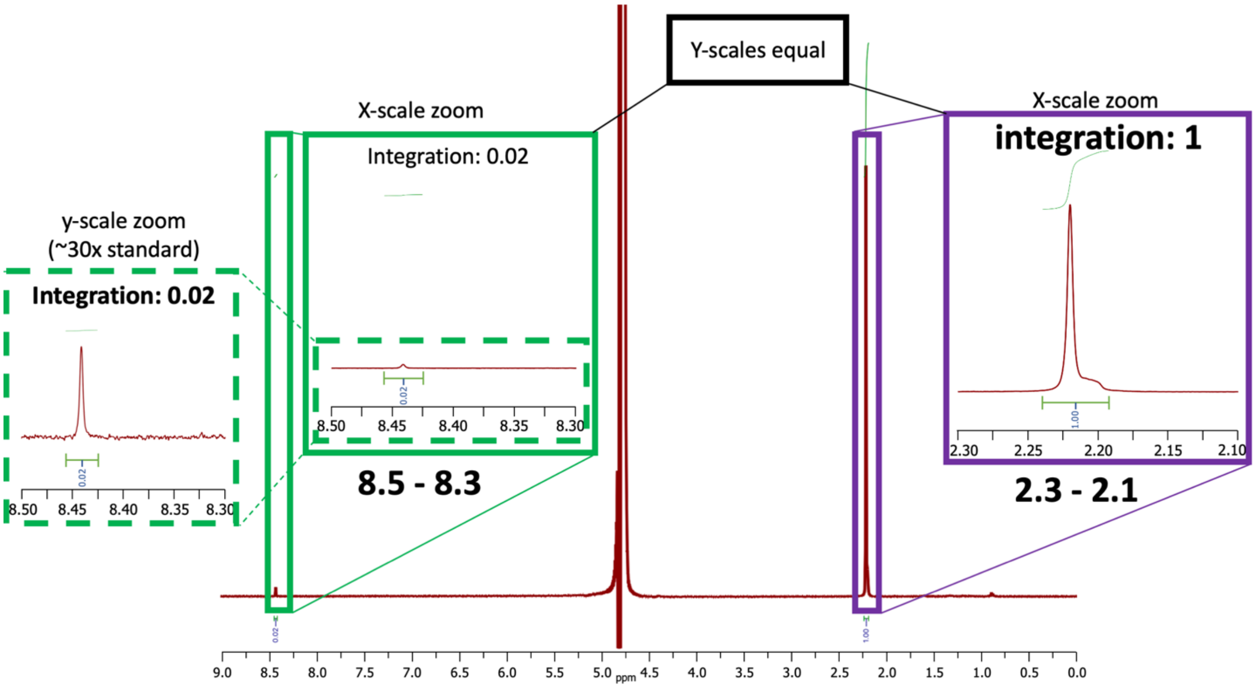

Both samples indicate formate above the detection limit, but below the limit of quantification (see section 6). A small broad peak in the alkyl region (2.19–2.21 ppm), observed also in Figure S14, Figure S15 and Figure S19, will require further analysis.

Figure S19. ^{1}H NMR spectra of Experiment 15 (only $NiCl_2$ in ocean precipitation fluid)

$FeCl_2$ was removed from the ocean precipitation fluid. $NiCl_2$ concentration was increased to 55 mM (up from 5 mM) to compensate for the missing 50 mM $FeCl_2$.

Acetone 0.6 μM was added as an internal standard.

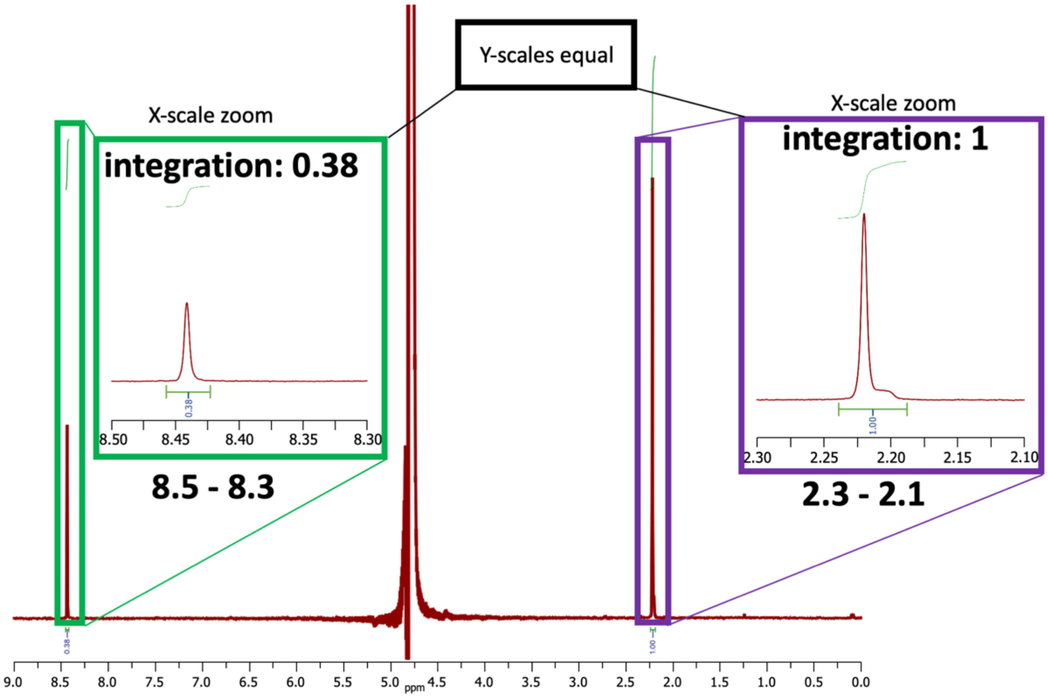

Integration of the acetone peak (1.00; 6 protons) relative to the formyl peak (0.38; 1 proton), indicates a formate concentration of 1.4 μM.

A small broad peak in the alkyl region (2.19–2.21 ppm), observed also in Figure S14, Figure S15 and Figure S18, will require further analysis.

Figure S20. ^{1}H NMR spectra of Experiment 16 (neither $FeCl_2$ nor $NiCl_2$, i.e. no precipitate)
By removing both $FeCl_2$ and $NiCl_2$ from the ocean precipitation fluid, no precipitate was formed.

Acetone 0.6 μM was added as an internal standard.

(A) No formate peak was observed.

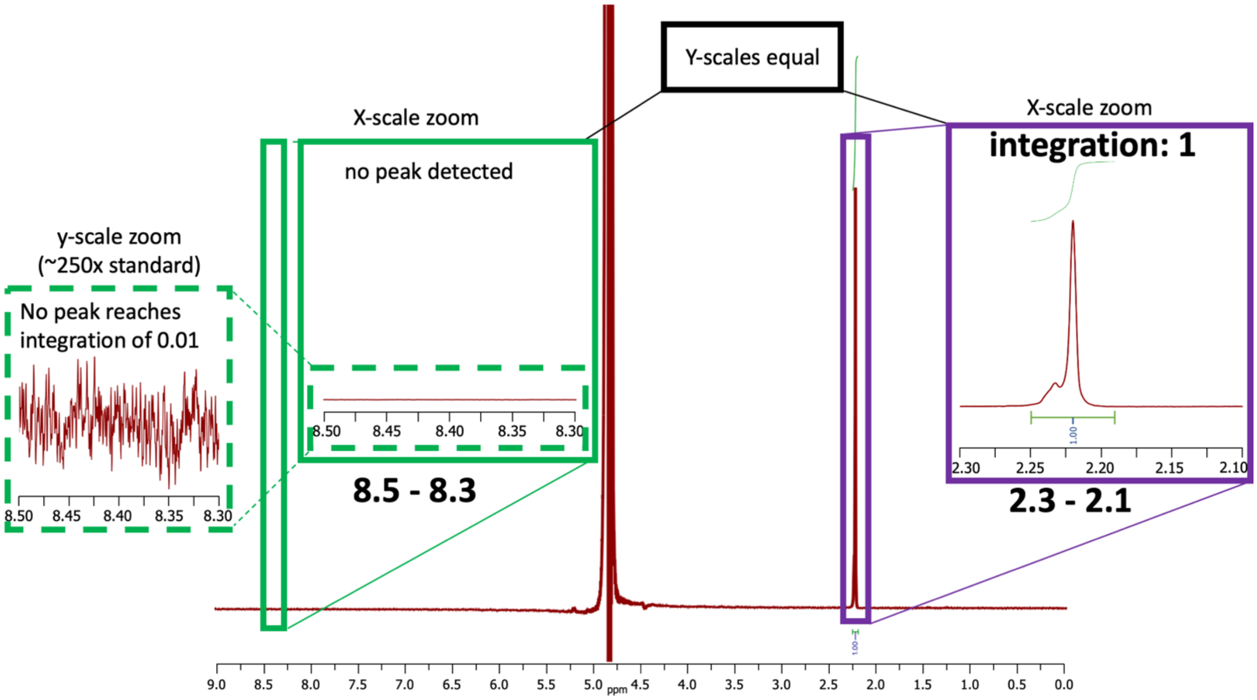

(B) Duplicate. No formate peak was observed.

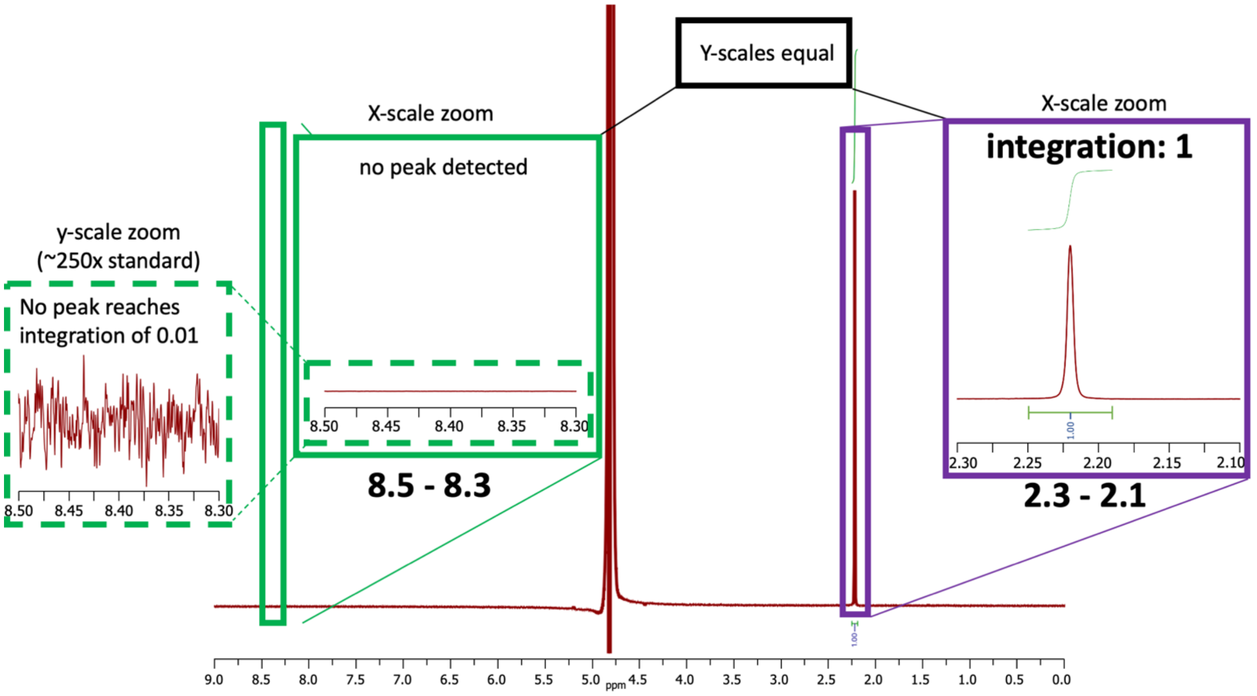

6. ^{1}H NMR determination of the Limit of Quantification (LoQ)

Table S2. Standard curve for quantification of formate with acetone as internal standard

The Limit of Quantification (LoQ) was determined by generating a standard curve of formate relative to a constant concentration of acetone.

[acetone] (μM)	acetone integration	formate integration	actual [formate] (μM)	Calc. [formate] (relative to acetone integration)	Quantifiable?
0.6	1	3.33	12 match→	← match 11.98	>LoQ
0.6	1	1.03	3.7 match→	← match 3.71	
0.6	1	0.11	0.37 match→	← match 0.39	LoQ
0.6	1	0.04	0.037 no match→	← no match 0.14	<LoQ
0.6	1	0.01	0.0037 no match→	← no match 0.036	

For the top 3 points, the calculated concentration of formate (relative to the acetone internal standard) matches the actual concentration of formate. For the bottom two points, the calculated concentration of formate no longer corresponds to the actual concentration of formate. The limit of quantification (LoQ) is therefore determined to be the most dilute solution of formate (0.37 μM) where the concentration can be reliably calculated by comparison to the acetone internal standard.

7. NMR – Technical details of water suppression

Below are the relevant parameters for our NMR experiments with water suppression.

Experiment:

Pulse Program: noesygppr1d
AQ_mod: DQD
TD: 32768
DS: 2
NS: 256
TD0: 1

Receiver:

RG: 48.8281
DW [μsec]: 48.000
DWOV [μsec]: 0.025
DECIM: 1920
DSPFIRM: sharp(standard)
DIGTYP: DRX
DIGMOD: baseopt
DR: 32
DDR: 0
DE [μsec]: 6.50
FILCOR [μsec]: 0
HPPRGN: normal
PH_ref [degree]: 0
OVERFLW: check

Nucleus 1:

NUC1: 1H
O1 [Hz]: 2344.87
O1P [ppm]: 4.692

SFO1 [MHz]: 499.7523449

BF1 [MHz]: 499.7500000

Durations:

Pulse [μsec]:

P[0]: 8.000

P[1]: 8.000

P[2]: 16.000

P[5]: 19.800

P[6]: 30.000

P[7]: 60.000

P[8]: 20000.000

P[11]: 80000.000

P[12]: 80000.000

P[13]: 1000.000

P[16]: 1000.000

P[17]: 2500.000

P[18]: 100000.000

P[19]: 600.000

P[25]: 216.000

P[26]: 100000.000

P[32]: 20000.000

P[40]: 2000.000

P[44]: 240.000

P[46]: 80000.000

P[47]: 46600.000

P[48]: 10000.000

P[50]: 80000.000

Delays [sec]:

D[1]: 20.00000000

D[8]: 0.010000000

D[16]: 0.000200000

Power:

Power Level [Watt]:

PLW[1]: 24.359

PLW[9]: 6.2359×10^{-5}

PLW[10]: 1.7322

PLW[11]: 0.12884

PLW[18]: 24.359

PLW[19]: 0.24359

PLW[27]: 0.13366

PLW[29]: 1.7322

PLW[32]: 2.4944×10^{-6}

Power Level [dB]:

PLdB[1]: -13.87

PLdB [9]: 42.05

PLdB [10]: -2.39

PLdB [11]: 8.9

PLdB [18]: -13.87

PLdB [19]: 6.13

PLdB [27]: 8.74

PLdB [29]: -2.39

PLdB [32]: 56.03

8. Reactor chip and precipitate images

Figure S21. Reactor chip and precipitate images

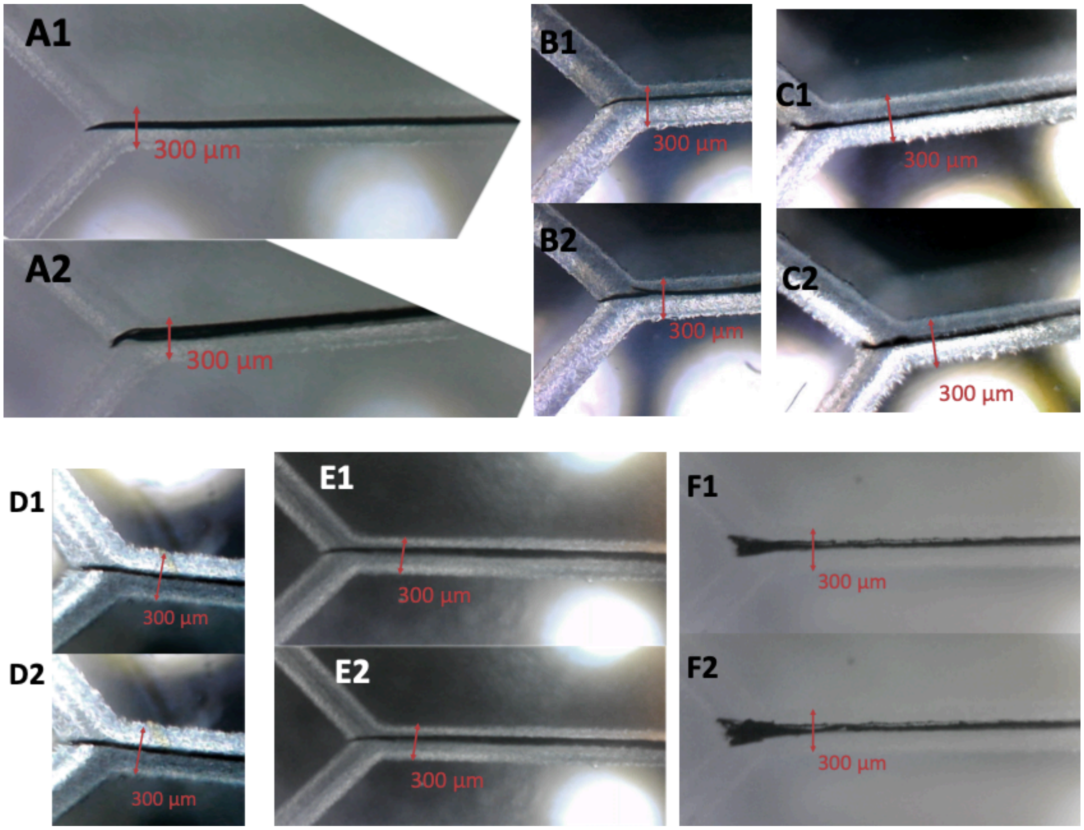

- **(A)** Precipitate before (A1) and after (A2) the reaction in experiment #1 (standard reaction and precipitation conditions).
- **(B)** Precipitate before (B1) and after (B2) the reaction in experiment #8 (standard precipitation conditions, but with the vent-side solution titrated to a pH of 3.9 during the post-precipitation conditions.
- **(C)** Precipitate before (C1) and after (C2) the reaction for experiment #11 (standard precipitation conditions, but with Na_2S as the only vent-side solute post-precipitation).
- **(D)** Precipitate before (D1) and after (D2) the reaction in experiment #13 (standard precipitation conditions, but with K_3PO_4 as the only vent-side solute post-precipitation).
- **(E)** Precipitate before (E1) and after (E2) the reaction for experiment #12 (standard precipitation conditions, but with K_2HPO_4 as the only vent-side solute during the reaction)
- **(F)** Precipitate before (F1) and after (F2) the reaction for experiment #15 (precipitation conditions in which $NiCl_2$ is the only ocean-side metal solute during the precipitation, and otherwise standard reaction solutes).

9. Depictions of plausible alternative CO_2-reduction mechanisms

As summarized in Figure 3, multiple mechanisms are plausible for the H_2-powered reduction of CO_2 that we have observed here. In this following section we discuss a number of them and why we conclude that none of them are more likely than the electrochemical mechanism that we have proposed in Figure 1A of the main text.

Figure S22. Classical hydrogenation – CO_2 permeability

In a system with high gas permeability, CO_2 could permeate from the ocean side to the vent side. Upon reaching the vent side, it could interact with dissociatively adsorbed surface and subsurface atomic H (originating from the H_2-rich vent fluids).

Passing across the precipitate: CO_2 (from the ocean to the vent side, through a pore).

Plausibility (given isotopic labeling results): Highly unlikely. Our isotopic labeling experiments indicate that the formyl H on the produced formate derives not from the feed gas on the vent side (H_2/D_2), but instead specifically from the ocean-side water (H_2O/D_2O). Therefore, with our microfluidic system, such a mechanism is not possible.

Ionic Hydrogenation (alternative):

A putative ionic hydrogenation would proceed similarly to the above classical hydrogenation but, rather than dissociatively adsorbing on the precipitate as a pair of hydrogen atoms, the H_2 would formally reduce the precipitate by generating a hydride at the surface. The hydride would then transfer to the incoming CO_2.

Plausibility (given isotopic labeling results): Highly unlikely.

Possibility of H exchange with the solvent in direct hydrogenations

Adsorbed $H^{\cdot}$ or H^{-} in a classical or ionic hydrogenation, respectively, could in principle exchange with the surrounding aqueous environment, so that we lose the original isotopic signal (reference (12) in the main text). However, this would inevitably imply considerable mixing of the two fluids, with a correspondingly mixed H/D signal in the product that we do not observe.

Figure S23. Classical hydrogenation – H_2 permeability

In a system with high gas permeability, H_2 could permeate from the ocean side to the vent side. Upon reaching the vent side, it could interact with dissociatively adsorbed surface and subsurface atomic H (originating from the H_2-rich vent fluids).

Passing across the precipitate: H_2 (from the vent to the ocean side, through a pore).

Plausibility (given isotopic labeling results): Highly unlikely. As above, our isotopic labeling experiments indicate that the formyl H on the produced formate derives not from the feed gas (H_2/D_2), but instead specifically from the ocean-side water (H_2O/D_2O). Therefore, with our microfluidic system, such a mechanism seems impossible.

Ionic hydrogenation (alternative):

Following migration of H_2 to the acidic side, an ionic-hydrogenation mechanism would proceed via adsorption of a hydride at the surface of the precipitate with release of a proton into the surrounding fluid (instead of a homolytic adsorption of a pair of neutral hydrogen atoms). The hydride could then potentially exchange with the surrounding aqueous environment, confounding our isotopic signal.

Plausibility (given isotopic-labeling results): Highly unlikely. If D_2 in experiment #4 had migrated to the ocean side and then become absorbed into the precipitate, the bound deuteride could have exchanged with the local environment (H_2O), giving the unlabeled signal that we observe. However, the migration of the dissolved hydrogen to the opposite side must have involved considerable mixing of fluids. So, if this were the mechanism, in experiment #5 we would have generated a mixture of H_2O and D_2O, with the corresponding $DCOO^-$ and $HCOO^-$ (representing a mixture of exchanged and unexchanged hydrides) in the product. Instead, we observe only $DCOO^-$, suggesting that the fluids did not significantly mix prior to reaction.

Figure S24. Classical hydrogenation – passage of dissociated atomic H

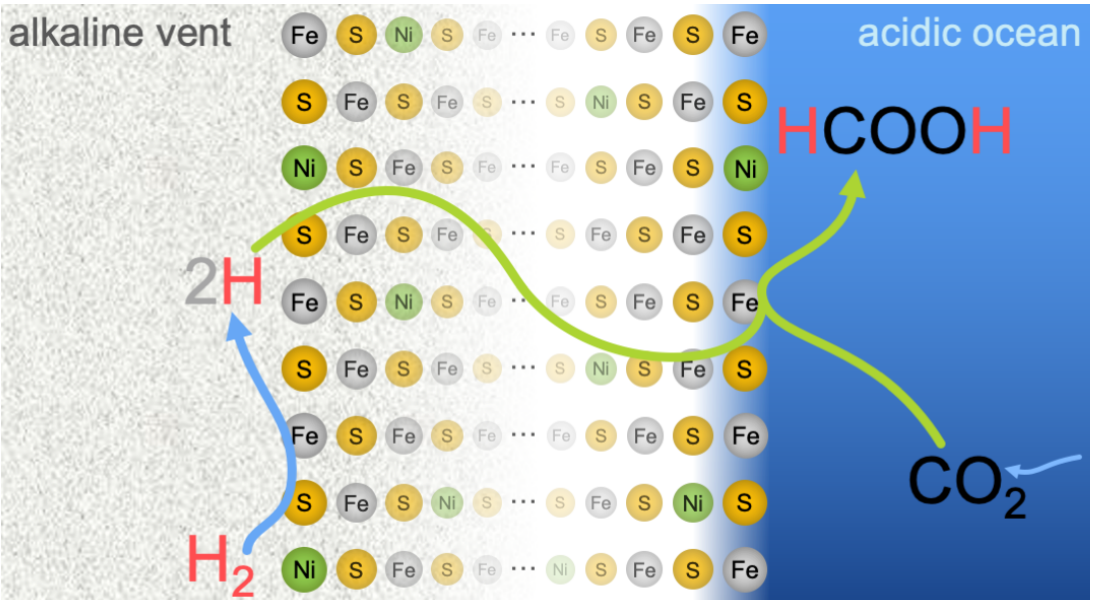

In a system with low gas permeability, H_2 could dissociatively adsorb on the vent side, and the atomic H could travel through the lattice of the precipitate to interact with CO_2 on the ocean side, where it could reduce CO_2 in classical hydrogenation.

Passing across the precipitate: Dissociated atomic H (from the vent to the ocean side, through the precipitate network itself).

Plausibility (given isotopic labeling results): Highly unlikely.

Once again, our isotopic labeling experiments indicate that the formyl H on the produced formate derives not from the feed gas (H_2/D_2), but instead specifically from the ocean-side water (H_2O/D_2O). Therefore, with our microfluidic system, such a mechanism seems impossible.

<u>Ionic hydrogenation (alternative):</u>

This proposed ionic hydrogenation would proceed similarly to the above classical hydrogenation but, rather than dissociatively adsorbing, the H_2 could formally reduce the precipitate by generating a hydride bound at the surface. The hydride could then potentially migrate to the ocean side, where it would exchange with the surrounding aqueous environment.

Plausibility (given isotopic labeling results): Highly unlikely. Again, hydride exchange with the local environment (D_2O on the ocean side) could explain the coupling of the formyl H/D signal with that of the ocean side water (DCOO when ocean side water is D_2O), but this would likely generate a mixture of $DCOO^-$ and $HCOO^-$ (representing a mixture of exchanged and unexchanged hydrides from the considerable mixing of H_2O and D_2O in experiment #5).

Figure S25. Localized redox cycling – CO_2 and H^+ permeability

This mechanism relies on redox cycling of corner or edge Ni or Fe atoms ($M^{2+} \rightleftarrows M^0$) on the vent side wherein H_2 oxidation is decoupled from CO_2 reduction. In such a scenario, the 'H' incorporated into the formate would derive from the acidic ocean side rather than from H_2. In this scenario, we consider H^+ passing from the acidic ocean side to the alkaline vent side through hydrated microchannels.

Passing across the precipitate: CO_2 and H^+ (from the ocean to the vent side, both through a pore). Passage of H^+ through a hydrated microchannel would involve rapid equilibration with the surrounding water. The resulting H^+ ions should thus take on more of the deuterated isotopic make-up of the vent-side fluid as they got closer to the vent side in our experiments with D_2 as a driver gas for the vent fluid. This mechanism should therefore result in at least a mixture of $HCOO^-$ and $DCOO^-$, which we do not observe (we observe pure $HCOO^-$).

As mentioned in the main text, we never added acids to the ocean side; the acidic pH (typically 3.9) was achieved solely by dissolution of CO_2 in water. Thus, in the experiments with D_2O as ocean-side solvent, all ocean-side protons must derive from the dissociation of carbonic acid via:

$$D_2O + CO_2 \rightleftharpoons D_2CO_3 \rightleftharpoons \mathbf{D^+} + DCO_3^-$$

Plausibility (given isotopic labeling results): Highly unlikely. We would have observed a mixed D/H signal (or in fact mostly H since H_2O was the prevalent fluid in the vent side) in experiment #5.

Figure S26. Localized redox cycling – CO_2 permeability and H^+ conductivity

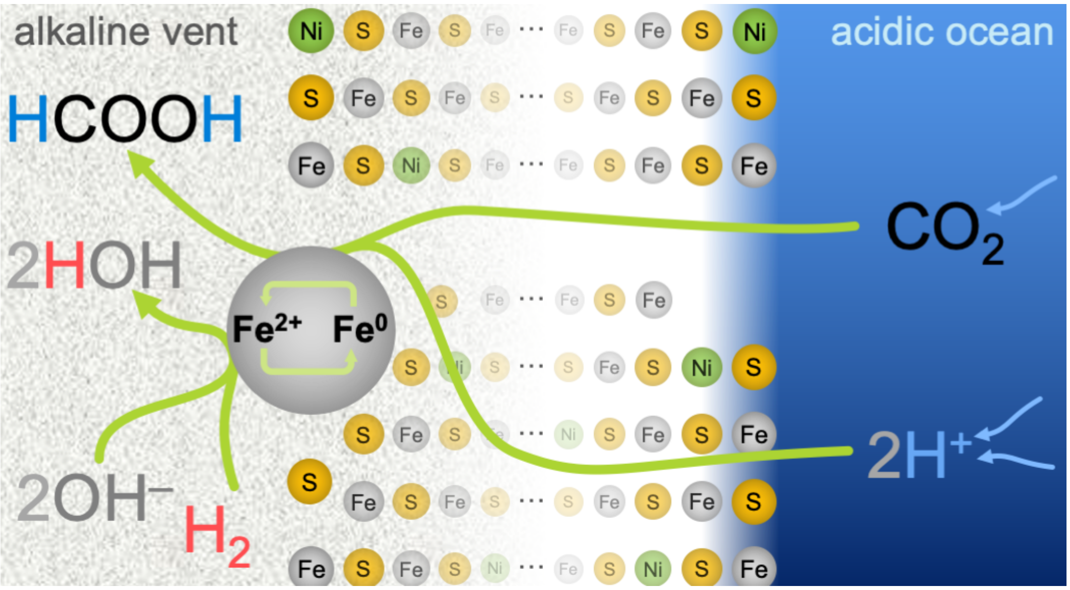

As in Figure S25, this mechanism relies on redox cycling of edge Ni or Fe atoms ($M^{2+} \rightleftarrows M^0$) on the vent side, with H_2 oxidation decoupled from CO_2 reduction. In such a scenario the 'H' incorporated into formate derives from the ocean side rather than from the H^+ generated by H_2 oxidation on the vent side. This would account for our observed deuterated product with D_2O as the solvent in the acidic fluid (and H_2O in the vent fluid). In contrast with Figure S25, in this scenario we consider H^+ passing from the acidic ocean side to the alkaline vent side via anhydrous proton conduction through the precipitate lattice.

Passing across the precipitate: CO_2 (from the ocean to the vent side, through a hydrated pore). H^+ (from the ocean to the vent side, anhydrously through the precipitate network itself).

In an anhydrous proton-conduction mode, protons would not equilibrate with the surrounding aqueous environment, allowing for the observed $HCOO^-$ in the experiments with D_2 as vent driver. However, it seems highly unlikely that our precipitates could be aqueous and porous enough to permit dissolved CO_2 to migrate to the alkaline side, but simultaneously have anhydrous enough sections to allow for dry proton conduction without equilibration to surrounding D_2O (in the experiments with D_2O as vent solvent).

Separately, our results indicate the need for a large pH gradient between the two semi-reactions. Keeping such a gradient at the nano-scale seems unlikely, but remains an open question (see the discussion in reference (6) in the main article).

Plausibility (given isotopic labeling results and need for pH gradient): Possible, but unlikely.

Figure S27. Localized redox cycling – H_2 permeability

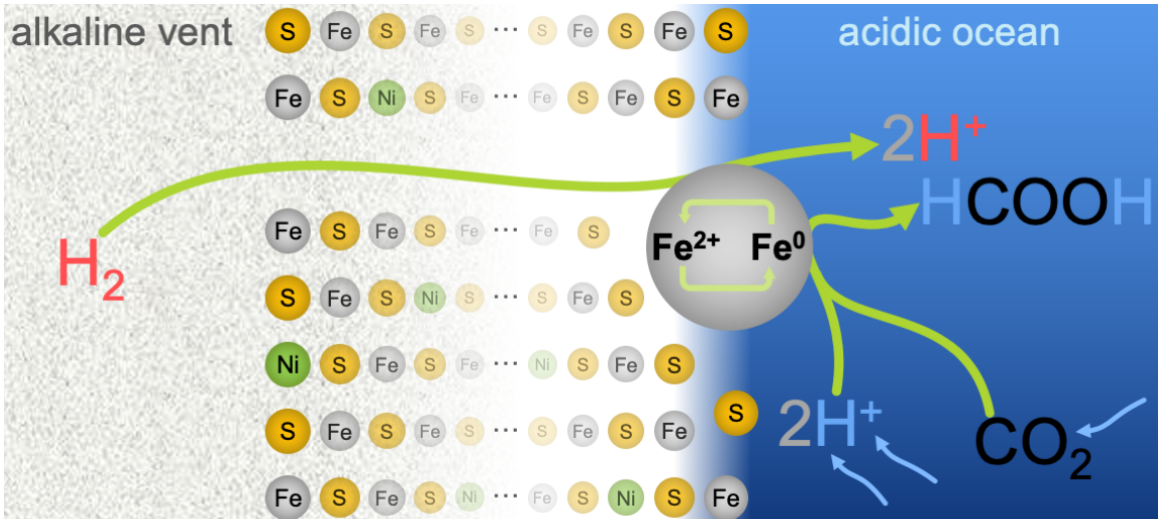

This mechanism relies on a redox cycling of corner or edge Ni or Fe atoms ($M^{II} \leftarrow\rightarrow M^0$) on the ocean side wherein H_2 oxidation is decoupled from CO_2 reduction. In such a scenario the 'H' incorporated into the formate would derive from the acidic ocean side rather than the H^+ generated from H_2 oxidation.

Passing across the precipitate: H_2 (from the vent to the ocean side).

This mechanism would agree with our isotopic results, assuming the pair of protons (H^+) released from the initial H_2 oxidation fully diffuse away before the CO_2 reacts with a fresh pair taken from the surroundings (otherwise we should have detected deuterated product when pushing the vent fluid with D_2). However, this mechanism would require H_2 oxidation on the ocean side, which is far less favorable than on the vent side, so we deem this process unlikely in our system.

Plausibility (given isotopic labeling results and need for pH gradient): Possible, but unlikely.

In conclusion, an electrochemical mechanism (main text, Figure 1A) seems the most likely mechanistic scenario, avoiding the implausibilities of the various classical and transfer hydrogenation alternatives described above.

10. Finite-element computer simulation of Venturi flow in a hydrothermal pore

We modeled a microfluidic pore narrowing from 2 mm into a channel 300 µm wide, before expanding again. The narrow section is connected to a perpendicular side pore 200 µm in diameter, which is itself assumed to lead into a reservoir (such as the ocean in our case). The narrowing at the bottom causes a Bernoulli drop in pressure, which leads to Venturi pull from the side reservoir into the hydrothermal channel system (Figure S28).

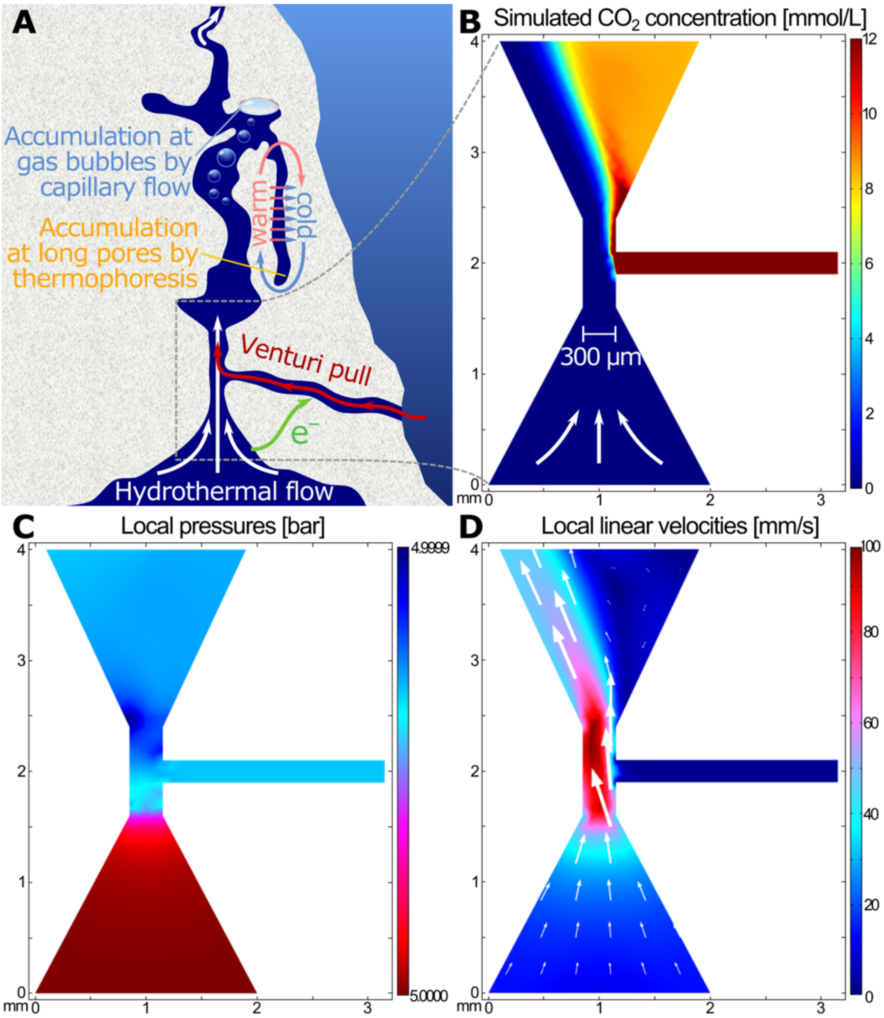

Figure S28. Simulation of hydrothermal-driven Venturi flow

(A) Narrowing of hydrothermal flow entering from the bottom causes a Bernoulli-principle drop in pressure, leading to Venturi pull from an open reservoir (e.g. ocean) connected to the side via a separate pore. Reagents (such as Fe^{2+}, CO$_2$ and H$^+$) could enter the microporous hydrothermal system in this way, and once inside react either with electrons (e$^-$) transferred through the electroconductive mineral, or upon meeting the hydrothermal flow at the center. Further up, thermal gradients at gas bubbles (13) and elongated pores (14, 15) can lead to concentration increases of any organics produced. **(B)** Steady-state finite-element simulation of concentration changes of CO_2 dissolved in a fluid entering from a side pore leading to a reservoir on the right (purported ocean). **(C)** Local pressures in the system. Even the minuscule 0.01% drop in pressure in the simulation here produces enough drag to pull fluids into the system, as shown in (B). **(D)** Local velocities in the system confirm the Bernoulli-principle behavior that leads to pull of fluids from the side pore.

As the H_2 dissolved in the hydrothermal fluid permeates upward through the vent, a decrease in pressure would lead to the spontaneous production of gas bubbles. A similar situation would occur as the CO_2 dissolved in the ocean was heated upon contact with the warmer vent fluid, releasing further gas bubbles. Flowing up, the bubbles would collect inside some of the vent's microchambers (Figure S28A, top center). At the gas-liquid interfaces, heated by the hydrothermal flow on one side and cooled by the ocean's proximity on the other, continuous capillary flow would facilitate vast increases in concentration and promotion of complex reactivity (13). Separately, the heat gradients would also cause thermal convection and diffusion at elongated pores, further increasing concentrations of organics by thermophoresis (14, 15) (Figure S28A, top right).

The finite-element computational simulation was performed in COMSOL Multiphysics v4.4 including the Laminar Flow and Transport of Diluted Species modules, with slip walls under a stationary solver with default options. The liquid was defined as incompressible. Temperature was defined uniformly as 75 ºC (323.15 K). Water-solvent and substance properties were set to COMSOL defaults. Pressure at the base of the hydrothermal system was defined as 5 bar (equivalent to ~40 m under sea level at present). To study the effect of Venturi pull, the pressures of the side pore and the top outlet were defined equal to each other, as 0.01% lower than the pressure of the hydrothermal inflow at the base.

The diffusion coefficient of CO_2 was calculated as described in (16) using:

$$D(CO_2) = D_0[T/T_s - 1]^m$$

where $D_0 = 13.942 \cdot 10^{-9}$ m^2/s; $T_s = 227.0$ K; and $m = 1.7094$.

11. Supplementary references

1. Maden BE (2000) Tetrahydrofolate and tetrahydromethanopterin compared: functionally distinct carriers in C1 metabolism. *Biochem J* 350(3):609–629.
2. Ragsdale SW, Pierce E (2008) Acetogenesis and the Wood-Ljungdahl pathway of CO_2 fixation. *Biochim Biophys Acta* 1784(12):1873–1898.
3. Yung YL, Russell MJ, Parkinson CD (2010) The search for life on mars. *J Cosmol* 5:1121–1130.
4. Herschy B, et al. (2014) An origin-of-life reactor to simulate alkaline hydrothermal vents. *J Mol Evol* 79:213–227.
5. Sojo V, Ohno A, McGlynn SE, Yamada YMA, Nakamura R (2019) Microfluidic reactors for carbon fixation under ambient-pressure alkaline-hydrothermal-vent conditions. *Life* 9(1):16.
6. Vasiliadou R, Dimov N, Szita N, Jordan S, Lane N (2019) Possible mechanisms of CO_2 reduction by H_2 via prebiotic vectorial electrochemistry. *Interface Focus* 9:20190073.
7. Möller FM, Kriegel F, Kieß M, Sojo V, Braun D (2017) Steep pH gradients and directed colloid transport in a microfluidic alkaline hydrothermal pore. *Angew Chemie Int Ed* 56(9):2340–2344.
8. Siever R (1992) The silica cycle in the Precambrian. *Geochim Cosmochim Acta* 56:3265–3272.
9. Mielke RE, et al. (2011) Iron-Sulfide-Bearing Chimneys as Potential Catalytic Energy Traps at Life's Emergence. *Astrobiology* 11(10):933–950.
10. Barge LM, et al. (2012) Characterization of iron-phosphate-silicate chemical garden structures. *Langmuir* 28(8):3714–3721.
11. Tosca NJ, Guggenheim S, Pufahl PK (2016) An authigenic origin for Precambrian greenalite: Implications for iron formation and the chemistry of ancient seawater. *Bull Geol Soc Am* 128(3–4):511–530.
12. Miller SL, Rittenberg D (1958) The catalysis of the H_2-D_2O exchange by aqueous buffer solutions. *J Am Chem Soc* 80(1):64–65.
13. Morasch M, et al. (2019) Heated gas bubbles enrich, crystallize, dry, phosphorylate and encapsulate prebiotic molecules. *Nat Chem* 11(9):779–788.
14. Duhr S, Braun D (2006) Why molecules move along a temperature gradient. *Proc Natl Acad Sci USA* 103(52):19678–19682.
15. Baaske P, et al. (2007) Extreme accumulation of nucleotides in simulated hydrothermal pore systems. *Proc Natl Acad Sci USA* 104(22):9346–9351.
16. Lu W, Guo H, Chou IM, Burruss RC, Li L (2013) Determination of diffusion coefficients of carbon dioxide in water between 268 and 473K in a high-pressure capillary optical cell with in situ Raman spectroscopic measurements. *Geochim Cosmochim Acta* 115:183–204.